

Detailed Abundances of 15 Stars in the Metal-Poor Globular Cluster NGC 4833*

Ian U. Roederer¹† and Ian B. Thompson²‡

¹*Department of Astronomy, University of Michigan, 1085 South University Avenue, Ann Arbor, MI 48109, USA*

²*Carnegie Observatories, 813 Santa Barbara Street, Pasadena, CA 91101, USA*

10 September 2021

ABSTRACT

We have observed 15 red giant stars in the relatively massive, metal-poor globular cluster NGC 4833 using the MIKE spectrograph at Magellan. We calculate stellar parameters for each star and perform a standard abundance analysis to derive abundances of 43 species of 39 elements, including 20 elements heavier than the iron group. We derive $\langle[\text{Fe}/\text{H}]\rangle = -2.25 \pm 0.02$ from Fe I lines and $\langle[\text{Fe}/\text{H}]\rangle = -2.19 \pm 0.013$ from Fe II lines. We confirm earlier results that found no internal metallicity spread in NGC 4833, and there are no significant star-to-star abundance dispersions among any elements in the iron group ($19 \leq Z \leq 30$). We recover the usual abundance variations among the light elements C, N, O, Na, Mg, Al, and possibly Si. The heavy-element distribution reflects enrichment by r -process nucleosynthesis ($[\text{Eu}/\text{Fe}] = +0.36 \pm 0.03$), as found in many other metal-poor globular clusters. We investigate small star-to-star variations found among the neutron-capture elements, and we conclude that these are probably not real variations. Upper limits on the Th abundance, $\log \epsilon(\text{Th}/\text{Eu}) < -0.47 \pm 0.09$, indicate that NGC 4833, like other globular clusters where Th has been studied, did not experience a so-called “actinide boost.”

Key words: globular clusters: individual (NGC 4833) — nuclear reactions, nucleosynthesis, abundances — stars: abundances — stars: Population II

1 INTRODUCTION

Globular clusters are the remnants of some of the most violent epochs of star formation in the history of the Universe. The compositions of the present-day stars provide a detailed chemical inventory to probe those ancient nucleosynthesis and enrichment events. Nevertheless, detailed chemical inventories for some Galactic globular clusters are still relatively unknown.

Only recently were the chemical compositions of a large sample of stars examined in one such cluster, NGC 4833 (Carretta et al. 2014). The properties and orbital parameters of NGC 4833 are listed in Table 1. NGC 4833 has one of the more extended, richly-populated blue horizontal branches among Galactic globular clusters (e.g., Menzies 1972; Samus et al. 1995; Melbourne et al. 2000; Piotto et al. 2002). This metal-poor cluster is a member of the “old” globular cluster population (e.g., Melbourne et al.;

Marín-Franch et al. 2009), and it ranks in the top quartile of most luminous clusters around the Milky Way (Harris 1996). The proper motion measurements and orbit calculations of Casetti-Dinescu et al. (2007) suggest that NGC 4833 and NGC 5986, another old and metal-poor cluster, share similar orbital characteristics. Casetti-Dinescu et al. suggested that these two clusters are dynamically associated and could be an accreted pair with a common origin in a now-disrupted satellite galaxy.

Until last year, the only high-resolution spectroscopic observations of stars in NGC 4833 had been conducted by Pilachowski, Sneden, & Wallerstein (1983), who observed two stars, Gratton & Ortolani (1989), who observed two stars, and Minniti et al. (1993, 1996), who observed one. These studies derived abundances of ≈ 15 –20 species in individual stars in NGC 4833, including O and Na abundances. They recognized that $[\text{O}/\text{Fe}]$ in some stars was depleted relative to the maximum $[\text{O}/\text{Fe}]$ ratios found in other clusters and field stars of similar metallicity. The small sample sizes limited these authors’ abilities to characterize the global chemical properties of NGC 4833. Carretta et al. (2014) observed 78 stars in NGC 4833 with the UVES and GIRAFFE spectrometers in the FLAMES instrument on the VLT.

* This paper includes data gathered with the 6.5 meter Magellan Telescopes located at Las Campanas Observatory, Chile.

† Email: iur@umich.edu

‡ Email: ian@obs.carnegiescience.edu

Table 1. Basic properties and orbital parameters of NGC 4833

Quantity	Symbol	Value	Reference
Right ascension	α (J2000)	12:59:34	1
Declination	δ (J2000)	−70:52:35	1
Galactic longitude	ℓ	303.6°	1
Galactic latitude	b	−8.0°	1
Luminosity	M_V	−8.17	1
Mass-to-light ratio	M/L	0.84 ± 0.45	2
Mass	M_*	$1.2 \times 10^5 M_\odot$	1
Central concentration	c	1.25	1
Distance modulus	$m - M$	15.05 ± 0.06	3
Distance from Sun	R_\odot	6.5 kpc	4
Distance from Galactic Center	$R_{G.C.}$	7.0 kpc	4
Perigalactic distance	R_{peri}	0.7 ± 0.2 kpc	4
Apogalactic distance	R_{apo}	7.7 ± 0.7 kpc	4
Maximum distance above Galactic plane	Z_{max}	1.8 ± 0.4 kpc	4
Orbital eccentricity	e	0.84 ± 0.03	4
Orbital period	T_{orbit}	91 ± 9 Myr	4

References: (1) Harris 1996; (2) Carretta et al. 2014; (3) Melbourne et al. 2000; (4) Casetti-Dinescu et al. 2007

This dataset enabled Carretta et al. to characterize the pattern of light-element (O, Na, Mg, Al, and Si) variations in NGC 4833. That study also characterized the abundances of 18 species of 15 heavier elements.

Carretta et al. (2014) presented several forms of evidence that suggest that NGC 4833 may have been tidally stripped more than the average cluster. First, NGC 4833 has a wide span of [Mg/Fe] ratios. This property has only been identified in a few massive or metal-poor clusters (Yong et al. 2005; Carretta et al. 2009b; Cohen & Kirby 2012), yet NGC 4833 is only the 36th most luminous Galactic globular cluster today. Second, NGC 4833 has an eccentric orbit, small perigalactic distance, and modest central concentration. These values predict a high destruction rate relative to other clusters (Casetti-Dinescu et al. 2007; Allen, Moreno, & Pichardo 2008). Third, the inner-quartile range of the [O/Na] ratios (IQR[O/Na]) in NGC 4833 lies on the upper envelope of clusters in the IQR[O/Na] versus luminosity correlation. Evidence discussed by Carretta et al. (2014) indicates that less-concentrated clusters of a given luminosity may have larger values of IQR[O/Na] and have lost more mass than more-concentrated ones. Finally, the low mass-to-light ratio of NGC 4833 hints that significant mass loss may have occurred as low-mass stars have been preferentially lost from the cluster. Carretta et al. (2014) note that no attempt has been made to detect these escaped stars as tidal tails, and potential investigators may have been intimidated by the stellar crowding and high reddening at the low Galactic latitude of NGC 4833. The preponderance of evidence suggests that NGC 4833 has lost a larger fraction of its initial stellar mass than the average Galactic globular cluster.

Our sample includes only 15 stars in NGC 4833, but our data cover most of the optical spectral range. We detect 43 species of 39 elements heavier than He, and this complements the more limited chemical inventory derived from a larger sample of stars studied by Carretta et al. (2014). These data enable us to focus new attention on the abundance pattern exhibited by the heaviest elements

in NGC 4833, those produced by neutron (n) capture reactions.

Throughout this work we adopt the standard definitions of elemental abundances and ratios. For element X, the logarithmic abundance is defined as the number of atoms of X per 10^{12} hydrogen atoms, $\log \epsilon(X) \equiv \log_{10}(N_X/N_H) + 12.0$. For elements X and Y, [X/Y] is the logarithmic abundance ratio relative to the solar ratio, defined as $\log_{10}(N_X/N_Y) - \log_{10}(N_X/N_Y)_\odot$, using like ionization states; i.e., neutrals with neutrals and ions with ions. We adopt the solar abundances listed in Asplund et al. (2009). Abundances or ratios denoted with the ionization state indicate the total elemental abundance as derived from transitions of that particular state.

2 OBSERVATIONS

We have observed 15 probable members of NGC 4833 with the Magellan Inamori Kyocera Echelle (MIKE) spectrograph (Bernstein et al. 2003) on the 6.5 m Landon Clay (Magellan II) Telescope at Las Campanas Observatory. Table 2 presents a log of these observations, and Figure 1 highlights these 15 stars on a color-magnitude diagram of NGC 4833. ThAr comparison lamp spectra have been taken immediately preceding or following each observation. The red and blue arms of MIKE are split by a dichroic at $\approx 4950\text{\AA}$. This setup provides complete wavelength coverage from 3350–9150 \AA . Data reduction, extraction, and wavelength calibration have been performed using the CARPY MIKE data reduction pipeline written by D. Kelson (see also Kelson 2003). Continuum normalization and order stitching have been performed within the IRAF environment.

Six stars were observed with the $0''.7 \times 5''.0$ slit. This setup yields a resolving power of $R \sim 41,400$ in the blue and $R \sim 36,300$ in the red, as measured from isolated ThAr lines in the extracted comparison lamp spectra. Nine stars were observed during poorer seeing conditions with the $1''.0 \times 5''.0$ slit, which yields a resolving power of $R \sim 30,500$ in the blue and $R \sim 25,900$ in the red. Table 3 presents signal-to-noise

Table 3. Photometry, model atmosphere parameters, and S/N ratios

Star ^a	Star ^b	Star ^c	V	$(B - V)_0$	$(V - K)_0$	T_{eff} (K)	$\log g$ [cgs]	v_t (km s ⁻¹)	[M/H]	S/N (3950 Å)	S/N (4550 Å)	S/N (5200 Å)	S/N (6750 Å)
2-185	D102	...	14.57	0.85	2.35	4670	1.55	1.75	-2.2	25	50	50	110
2-277	D109	...	14.90	0.87	2.26	4752	1.72	1.80	-2.2	25	50	50	110
2-882	D193	...	14.66	0.84	2.45	4665	1.57	1.70	-2.2	20	40	50	110
2-918	C49	33027	14.75	0.83	2.40	4696	1.63	1.85	-2.2	20	45	40	110
2-1578	C91	31836	14.12	0.89	2.26	4595	1.35	1.75	-2.2	30	50	60	140
2-1664	C92	...	14.34	0.86	2.82	4527	1.32	1.80	-2.2	35	75	75	180
3-742	C129	31370	13.60	1.05	2.91	4357	0.93	2.00	-2.2	25	65	75	200
3-772	D167	...	14.50	0.89	2.37	4647	1.50	1.65	-2.2	10	30	40	95
3-1509	C145	31929	14.38	0.87	2.52	4591	1.41	1.85	-2.2	20	45	50	120
4-224	D136	...	13.51	1.02	2.70	4385	0.96	2.05	-2.2	20	45	55	120
4-341	D135	...	13.56	1.05	2.69	4397	0.98	1.95	-2.2	40	95	110	250
4-464	D153	...	14.48	0.86	2.45	4628	1.48	1.90	-2.2	10	40	45	115
4-1255	D49	...	13.21	1.14	2.60	4344	0.84	2.15	-2.2	35	80	90	215
4-1398	C191	...	14.23	0.89	2.56	4556	1.33	1.85	-2.2	15	45	50	115
4-1706	D41	...	15.01	0.78	2.32	4764	1.76	1.85	-2.2	25	45	50	105

^a This study, based on Piotto et al. (2002)

^b Menzies (1972)

^c Carretta et al. (2014)

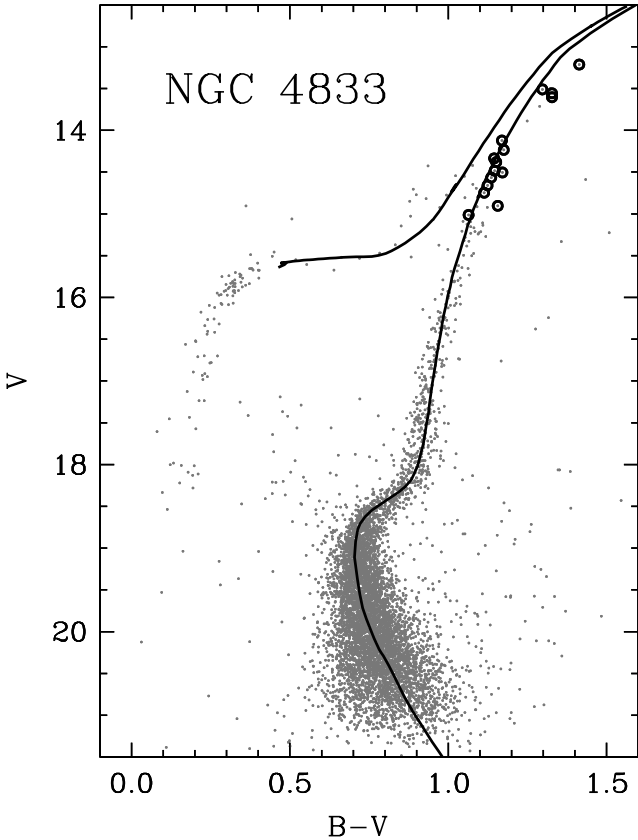


Figure 1. The $B - V$ versus V colour-magnitude diagram using photometry from Piotto et al. (2002). Stars observed with MIKE are marked with circles. The line is an isochrone from the PARSEC database (v. 1.2S; Bressan et al. 2012; Chen et al. 2014) computed for an age of 13 Gyr and metallicity $Z = 0.00025$. The isochrone is shifted to a distance modulus of 15.05 and a reddening of $E(B - V) = 0.32$.

Table 2. Observing log

Star	Slit	Date	UT _{start}	t_{exp} (s)	RV (km s ⁻¹)
2-185	1''0	2011 03 18	04:41	2600	211.0
2-277	1''0	2011 03 18	03:38	3600	201.7
2-882	1''0	2011 03 18	02:42	3200	209.8
2-918	1''0	2011 03 18	05:27	3000	209.8
2-1578	0''7	2011 03 17	02:52	5400	201.3
2-1578	0''7	2011 03 17	06:33	1800	201.2
2-1664	0''7	2011 03 17	04:30	7200	199.5
3-742	0''7	2011 01 31	07:43	2400	206.4
3-772	1''0	2011 03 17	23:40	2800	203.0
3-1509	1''0	2011 03 18	01:56	2400	207.4
4-224	0''7	2011 01 28	08:22	1200	201.5
4-341	0''7	2011 01 28	08:47	2400	202.2
4-341	0''7	2011 01 29	08:22	2400	202.5
4-464	1''0	2011 03 18	00:29	2600	297.6
4-1255	0''7	2011 01 31	08:29	2400	205.9
4-1398	1''0	2011 03 18	01:16	2200	200.1
4-1706	1''0	2011 03 18	06:20	3400	187.9

(S/N) estimates based on Poisson statistics for the number of photons collected per pixel in the continuum. These values are measured from the co-added spectra.

We adopt a star naming convention based on the Piotto et al. (2002) photometry files. This convention has the form “chip-ID.” The first value (“chip”) indicates the WFPC2 chip number, and the second value (“ID”) indicates the star identification number.

Figure 2 illustrates a 25 Å portion of the MIKE spectra of all 15 stars observed in our study. The spectra are sorted by increasing V -magnitude from top to bottom. Lines of nine species of six elements are marked. This illustrates the richness of blue spectra of red giant stars, even when the overall metallicity is less than 100 times the solar metallicity.

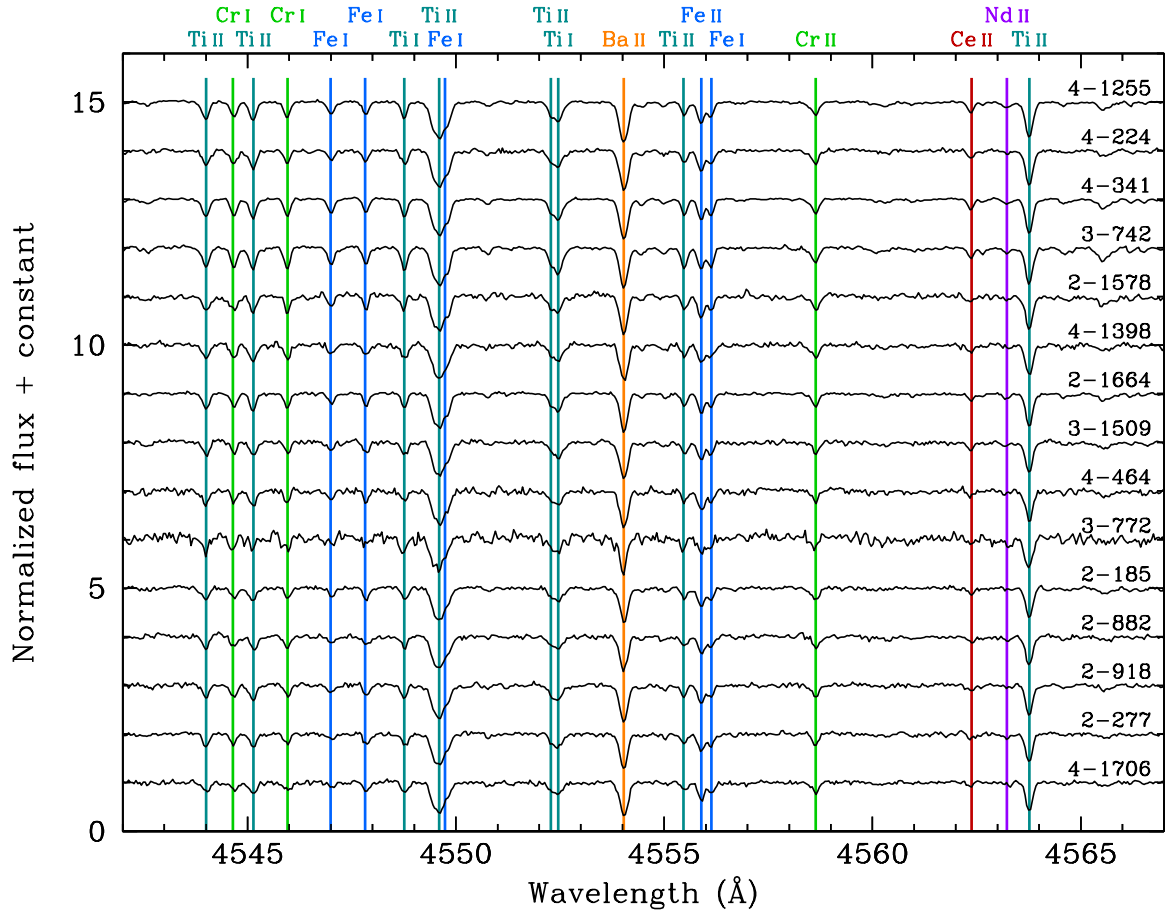


Figure 2. Small portions of the blue spectra of all 15 stars in our study. Identifications are given for 19 absorption lines. Velocity shifts have been removed, and the spectra have been shifted vertically for the sake of illustration. The stars are sorted by increasing V -magnitude from top to bottom.

3 RADIAL VELOCITIES

We measure the stellar radial velocity (RV) of each observation with respect to the ThAr lamp by cross-correlating the echelle order containing the Mg I b lines in each spectrum against a template using the *fxcor* task in IRAF. We create the template by measuring the wavelengths of unblended Fe I lines in this order in star 4-1255, which has the highest S/N in a single exposure. We compute velocity corrections to the Heliocentric rest frame using the IRAF *rvcorrect* task. This method yields a total uncertainty of $\approx 0.6 \text{ km s}^{-1}$ per observation (see Roederer et al. 2014). Table 2 presents the Heliocentric RV measured for each observation.

We derive a mean Heliocentric RV to NGC 4833 of $203.0 \pm 1.5 \text{ km s}^{-1}$ [s.e.m.] ($\sigma = 5.9 \text{ km s}^{-1}$ [s.d.]). All stars are within $2'$ of the cluster center, and the RV of each star is within 2.5σ of the systemic velocity. There is a high probability that all 15 stars observed are members of NGC 4833.

The mean heliocentric RV and dispersion of NGC 4833 have been derived from high resolution GIRAFFE spectra by two previous studies, Carretta et al. (2014) and Lardo et al. (2015). Carretta et al. reported a systemic velocity of $202.0 \pm 0.5 \text{ km s}^{-1}$ and a dispersion of $4.1 \pm 0.3 \text{ km s}^{-1}$ based on a sample of 78 stars. Lardo et al. reported a systemic velocity of $202.1 \pm 0.6 \text{ km s}^{-1}$ and a dispersion of 3.9 km s^{-1} based on a sample of 82 stars.

Our values are in agreement. These values are also in reasonable agreement with previous measurements derived from low-resolution spectra of smaller samples of stars in NGC 4833 by Geisler et al. (1995) ($201.0 \pm 1.3 \text{ km s}^{-1}$, $\sigma = 4.6 \text{ km s}^{-1}$, 12 stars) and Rutledge et al. (1997) ($194.1 \pm 7.5 \text{ km s}^{-1}$, $\sigma = 3.3 \text{ km s}^{-1}$, 26 stars). For completeness, we note that no abundances have been presented from the spectra presented by Lardo et al.

4 EQUIVALENT WIDTHS

We measure equivalent widths using a semi-automatic routine that fits Voigt absorption line profiles to the continuum-normalized spectra. Following the same methods discussed in Roederer et al. (2014), we inspect all equivalent width measurements by eye, and we make manual adjustments to the fits when necessary. Uncertainties in the equivalent widths are estimated based on the S/N ratios that vary as a function of wavelength. The complete list of equivalent widths is presented in Table 4, which is available in the Supplementary Information section found in the online edition of the journal. A short version is shown in the printed edition to illustrate its form and content.

We observed four stars in common with the GIRAFFE sample of Carretta et al. (2014). Those authors note that

Table 4. Atomic data and equivalent widths

Wavelength (Å)	Species ^a	E.P. (eV)	log <i>gf</i>	Ref.	2-185	...
6707.80	3.0	0.00	0.17	1	limit	...
6300.30	8.0	0.00	-9.78	2	limit	...
7771.94	8.0	9.14	0.37	2	limit	...
7774.17	8.0	9.14	0.22	2	limit	...
7775.39	8.0	9.14	0.00	2	limit	...
5682.63	11.0	2.10	-0.71	2	23.9	...
5688.20	11.0	2.10	-0.45	2	43.3	...
6154.22	11.0	2.10	-1.55	2
6160.75	11.0	2.10	-1.25	2	13.1	...
4702.99	12.0	4.33	-0.38	2	88.9	...
5528.40	12.0	4.34	-0.50	2	95.7	...
5711.09	12.0	4.34	-1.72	2	20.9	...
⋮	⋮	⋮	⋮	⋮	⋮	⋮

Notes.— The full version of Table 4 is available in the supplementary material online. Here, “synth” denotes lines used to derive an abundance via spectrum synthesis, and “limit” denotes lines used to derive an upper limit.

References.— (1) Smith, Lambert, & Nissen 1998; (2) Fuhr & Wiese 2009; (3) Aldenius, Lundberg, & Blackwell-Whitehead 2009; (4) Lawler & Dakin 1989, using HFS from Kurucz & Bell 1995; (5) Lawler et al. 2013; (6) Wood et al. 2013; (7) Doerr et al. 1985, using HFS from Kurucz & Bell 1995; (8) Wood et al. 2014b; (9) Sobek, Lawler, & Sneden 2007; (10) Nilsson et al. 2006; (11) Den Hartog et al. 2011 for both log *gf* value and HFS; (12) Ruffoni et al. 2014; (13) Fuhr & Wiese 2009, using HFS from Kurucz & Bell 1995; (14) Wood et al. 2014a; (15) Roederer & Lawler 2012; (16) Biémont et al. 2011; (17) Ljung et al. 2006; (18) Nilsson et al. 2010; (19) Palmeri et al. 2005; (20) Fuhr & Wiese 2009, using HFS/IS from McWilliam 1998 when available; (21) Lawler, Bonvallet, & Sneden 2001, using HFS from Ivans et al. 2006; (22) Roederer et al. 2011; (23) Lawler et al. 2009; (24) Li et al. 2007, using HFS from Sneden et al. 2009; (25) Ivarsson, Litzén, & Wahlgren 2001, using HFS from Sneden et al. 2009; (26) Den Hartog et al. 2003, using HFS/IS from Roederer et al. 2008 when available; (27) Lawler et al. 2006, using HFS/IS from Roederer et al. 2008 when available; (28) Lawler et al. 2001a, using HFS/IS from Ivans et al. 2006; (29) Den Hartog et al. 2006; (30) Roederer et al. 2012; (31) Lawler et al. 2001b, using HFS from Lawler, Wyart, & Blaise 2001 when available; (32) Wickliffe, Lawler, & Nave 2000; (33) Lawler, Sneden, & Cowan 2004 for both log *gf* value and HFS; (34) Lawler et al. 2008; (35) Wickliffe & Lawler 1997; (36) Sneden et al. 2009 for both log *gf* value and HFS/IS; (37) Lawler et al. 2007; (38) Ivarsson et al. 2003, using HFS/IS from Cowan et al. 2005—see note on log *gf* values there; (39) Biémont et al. 2000, using HFS/IS from Roederer et al. 2012; (40) Nilsson et al. 2002.

^a The number to the left of the decimal point indicates the atomic number, and the number to the right of the decimal point indicates the ionization state (0 = neutral, 1 = first ion)

equivalent widths measured from their GIRAFFE spectra are consistently larger than the equivalent widths measured from their higher-resolution UVES spectra. They adopt a linear transformation to convert their GIRAFFE equivalent widths to the UVES scale. We compare our measured equivalent widths with their corrected GIRAFFE equiva-

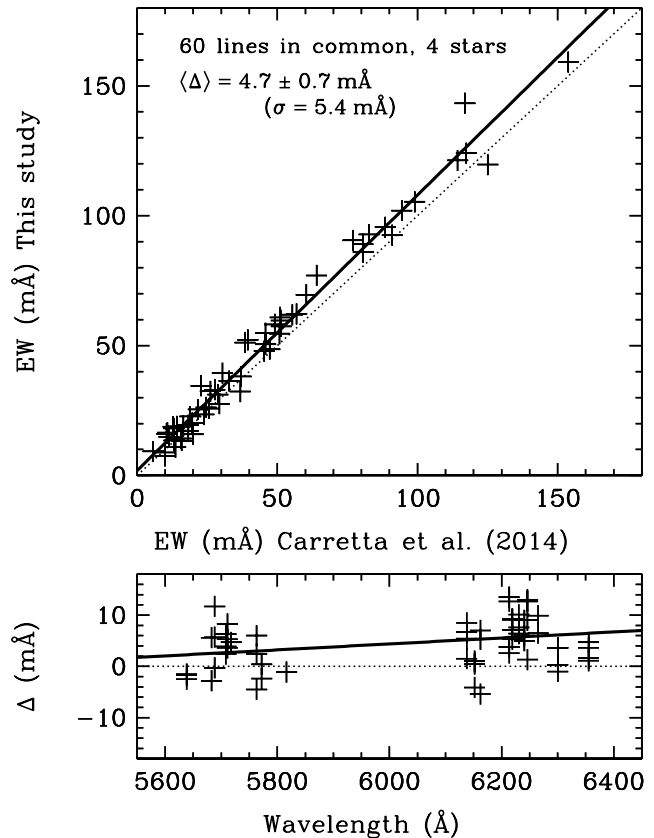


Figure 3. Comparison of equivalent widths measured by Carretta et al. (2014) and us for four stars in common. The top panel illustrates the equivalent widths, and the bottom panel illustrates the differences as a function of wavelength. The dotted lines represent a 1:1 correspondence, and the solid lines represent the linear fits.

lent widths. As illustrated in Figure 3, we find a difference of $+4.7 \pm 0.7 \text{ m\AA}$ ($\sigma = 5.4 \text{ m\AA}$) in the sense that our equivalent widths are larger. There is a slight trend with wavelength, but this is only significant at the 2σ level.

Carretta et al. (2007) note that the transformation from the GIRAFFE scale to the UVES scale is necessary to ensure agreement with equivalent widths measured independently by other investigators. Equivalent widths measured from their UVES spectra of stars in NGC 6752 are in reasonable agreement with those measured from $R \sim 110,000$ spectra obtained by Yong et al. (2003), $\langle \Delta \rangle = +1.7 \pm 0.4 \text{ m\AA}$ ($\sigma = 5.6 \text{ m\AA}$). Our equivalent width measurements are made with the same techniques and software used to examine hundreds of metal-poor stars observed with MIKE (Roederer et al. 2014). The CARPY software package used to extract the MIKE observations is also identical. Our previous work found excellent agreement among the equivalent widths measured from MIKE spectra and those measured from echelle data collected at McDonald Observatory. There was a difference of $+0.7 \pm 0.2 \text{ m\AA}$ ($\sigma = 4.0 \text{ m\AA}$) for the HRS on the Hobby-Eberly Telescope and a difference of $+1.0 \pm 0.1 \text{ m\AA}$ ($\sigma = 3.7 \text{ m\AA}$) for the Tull Coudé Spectrograph on the Harlan J. Smith Telescope. Furthermore, Roederer et al. made extensive comparisons between the equivalent widths for weak lines in stars in common with Carretta et al. (2002), Johnson (2002), Ivans et al. (2003),

Cayrel et al. (2004), Honda et al. (2004), and Lai et al. (2008). The offsets were all ≤ 1.3 mÅ. Thus we conclude that equivalent widths measured from MIKE spectra taken with the 0".7 slit are not systematically in error.

We also investigate whether the wider MIKE slit used for some of our observations may be the source of this difference. Two of the four stars in NGC 4833 in common with Carretta et al. (2014) were observed using the 0".7 slit, and two were observed using the 1".0 slit. The mean difference is $+4.5 \pm 1.1$ mÅ ($\sigma = 6.2$ mÅ) for the two stars observed with the 0".7 slit and $+4.8 \pm 0.8$ mÅ ($\sigma = 4.6$ mÅ) for the two stars observed with the 1".0 slit. The difference is not significant, and we conclude that the different slits are not the source of the discrepancy.

In principle, poor sky subtraction could result in a systematic bias in the equivalent widths measured from a single night. The four stars in common with Carretta et al. (2014) were observed on three different nights. Star 3-742 was observed on 2011 01 31, when the moon was only 6 per cent illuminated and 69° away from NGC 4833. The other three stars were observed on 2011 03 17 and 2011 03 18, when the moon was >90 per cent illuminated and $>78^\circ$ away from NGC 4833. The mean difference is $+5.6 \pm 1.6$ mÅ ($\sigma = 6.7$ mÅ) for the observations near new moon and $+4.2 \pm 0.7$ mÅ ($\sigma = 4.6$ mÅ) for the observations near full moon. The difference is not significant, and we conclude that poor sky subtraction is not the source of the discrepancy.

Finally, we note that Roederer, Marino, & Sneden (2011) examined spectra of several stars in globular cluster M22 that were taken on the same two nights in March, 2011. That study compared the equivalent widths measured in those stars with those measured by Marino et al. (2011). Again, the offset is small, $\langle \Delta \rangle = +1.8 \pm 0.3$ mÅ ($\sigma = 3.7$ mÅ). There is no compelling evidence that our MIKE observations of M22 or NGC 4833 conducted in March, 2011, are contaminated by the solar spectrum reflected by the full moon.

In conclusion, we cannot explain the 4.7 mÅ offset in the mean equivalent width differences between our data and that of Carretta et al. (2014). In Section 6.2, we find that the cumulative effect of the choice of Fe I lines used for the analysis, the $\log gf$ values, and this equivalent width difference is 0.04 dex. This value is relatively small, and we do not pursue the matter further.

5 BROADBAND PHOTOMETRY AND REDDENING

Table 3 presents the photometry and colours. V and $(B - V)$ are taken from Piotto et al. (2002)¹ and have been transformed by those authors to the Johnson system from their *Hubble Space Telescope* (HST) WFPC2 F439W and F555W broadband photometry. K magnitudes are taken from the Two-Micron All Sky Survey (2MASS; Skrutskie et al. 2006). The $(B - V)$ and $(V - K)$ colours are dereddened according to the differential reddening maps of Melbourne et al. (2000) and the extinction coefficients of Cardelli et al. (1989). All

¹ Downloaded from <http://www.astro.unipd.it/globulars/> on 2010 October 22

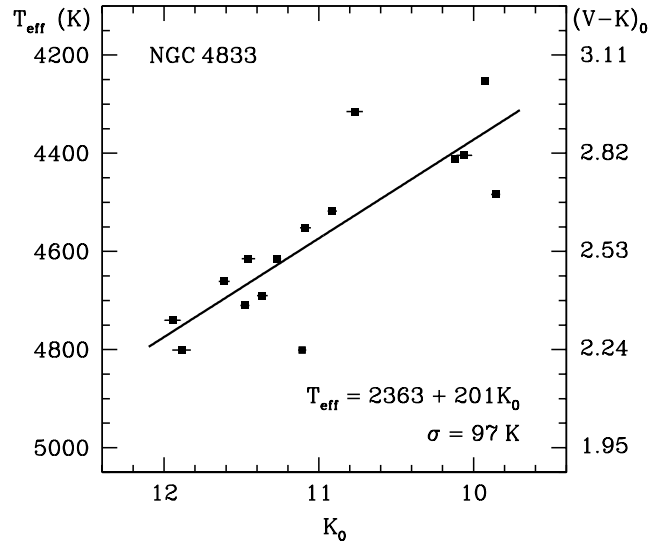


Figure 4. Relationship between dereddened K magnitudes and T_{eff} predicted by dereddened $(V - K)$ colours, which are approximated on the right axis for reference. The linear least-squares fit is shown.

15 stars that we have observed are within $2'$ of the cluster center, and the full range of reddening for these stars is $0.310 \leq E(B - V) \leq 0.322$ according to the Melbourne et al. maps. The differential reddening is a small effect compared to the relatively large extinction toward NGC 4833 at low Galactic latitude ($b = -8^\circ$).

6 MODEL ATMOSPHERES

We interpolate model atmospheres from the ATLAS9 α -enhanced grid (Castelli & Kurucz 2003). We use a recent version of the line analysis code MOOG (Sneden 1973; see also Sobeck et al. 2011), operated in batch mode, to perform the analysis. In Section 6.1, we discuss our methods to estimate the appropriate model atmosphere parameters. We compare these values with those derived by Carretta et al. (2014) in Section 6.2.

6.1 Model parameters

We first estimate the stellar effective temperature (T_{eff}) using the metallicity-dependent $V - K$ colour- T_{eff} relations of Alonso et al. (1999b). We transform the K magnitudes from the 2MASS system to the TCS system according to Equation 5 of Ramírez & Meléndez (2005). We refine the initial estimate by fitting a line to the relation between dereddened K magnitude, K_0 , and T_{eff} calculated from $(V - K)_0$. Figure 4 illustrates this relationship. The standard deviation of the residuals with respect to this fit is 97 K, which we adopt as the uncertainty in T_{eff} for each star.

The two stars that deviate most from the fit are 2-1578 and 2-1664. Both stars are within $2'$ of the cluster center, as are most other stars in our sample. No neighboring stars within 5 magnitudes and 10 pixels are found in the Piotto et al. (2002) photometry files, and no faint contaminants are apparent in the WFPC2 images. No photometry error flags are reported for either star. The $(V - K)_0$ colors

of these stars would need to be different by about +0.2 mag and -0.2 mag, respectively, to bring each star to the best-fit line in Figure 4. These stars are only about 11'' apart, so it is highly unlikely that differential reddening is underestimated for one and overestimated for the other. We derive metallicities of these two stars ($[\text{Fe I}/\text{H}] = -2.23$ and -2.24 , $[\text{Fe II}/\text{H}] = -2.23$ and -2.18 , respectively; Section 8) that are in excellent agreement with the cluster means. In summary, we find no reason to exclude either star when computing the standard deviation of the residuals to the fit shown in Figure 4.

Uncertainties in K_0 translate to uncertainties of only 33 K in T_{eff} on average. Small changes in the differential reddening across the face of NGC 4833 have a minimal effect on T_{eff} when derived this way. $A(K)/E(B - V) \approx 0.35$ (Cardelli et al. 1989), so a differential reddening of ± 0.012 mag in $E(B - V)$ (Melbourne et al. 2000) translates to ± 0.004 mag in K . The slope of the $T_{\text{eff}}-K_0$ relation shown in Figure 4 is 201 K/mag. Thus differential reddening contributes an average of ≈ 1 K to the T_{eff} uncertainty budget, which is negligible. We assume that all giants in NGC 4833 reside along a single red giant branch (RGB) fiducial with $[\text{Fe}/\text{H}] = -2.2$ (Section 9.1). A change in $[\text{Fe}/\text{H}]$ of 0.1 dex affects the calculated T_{eff} values by < 1 K, which is also negligible.

Melbourne et al. (2000) derived the distance to NGC 4833 using the absolute magnitudes of RR Lyrae variables along the horizontal branch (HB). We use this distance, $(m - M) = 15.05 \pm 0.06$, to derive the surface gravities ($\log g$) for all 15 stars observed from the fundamental relation $\log g = 4 \log(T_{\text{eff},*}) - \log(M/M_{\odot}) - 0.4(M_{\text{bol},\odot} - M_{\text{bol},*}) - 10.61$. Here, $M_{\text{bol},*} = \text{BC}_K + m_K - (m - M)$, and the constant 10.61 is derived from the solar values given in Cox (2000). We assume a mass of $0.8 M_{\odot}$ for all stars on the RGB in NGC 4833. We interpolate BC_K from the grid of bolometric corrections presented by Alonso et al. (1999a). Uncertainties of 0.05 in magnitude, 97 K in T_{eff} , $0.1 M_{\odot}$ in mass, and 0.06 in the distance modulus only affect the derived $\log g$ values by 0.02, 0.04, 0.05, and 0.03 dex, respectively. Their collective uncertainties contribute a total of 0.07 dex uncertainty in $\log g$.

We derive the microturbulent velocity, v_t , by minimizing correlations between the equivalent width (expressed as the log of the equivalent width divided by λ) of Fe I lines and the abundances derived from them. The internal uncertainty associated with this method is ≈ 0.05 dex.

Finally, we assign a single metallicity to all model atmospheres, $[\text{Fe}/\text{H}] = -2.2$. This is justified by our results indicating that NGC 4833 is mono-metallic and has a mean metallicity of $[\text{Fe II}/\text{H}] = -2.19 \pm 0.013$ (Section 9.1). Our use of the α -enhanced grid of models is justified because the most abundant electron-donating metals are enhanced by factors of a few relative to Fe in NGC 4833 when compared with the solar ratios.

6.2 Comparison with Carretta et al.

Carretta et al. (2014) used a procedure similar to ours to derive their T_{eff} values for stars in NGC 4833. Their procedure is discussed in detail by Gratton et al. (2007). There are four stars in common between our study and theirs, and we derive a mean difference in T_{eff} of -28 ± 1 K ($\sigma = 2$ K).

Both studies use the same 2MASS K magnitudes to calculate T_{eff} after computing a relation like that shown in Figure 4. There appears to be a zeropoint offset in the V magnitudes used to compute the initial relationship between $V - K$ and T_{eff} . We adopt V magnitudes from Piotto et al. (2002), who calibrated their *HST* $F555W$ magnitudes to V in the standard Johnson system. Carretta et al. used their own ground-based V magnitudes calibrated with an absolute zeropoint uncertainty of 0.03 mag. A systematic zeropoint difference of ± 0.03 mag translates to an average difference in T_{eff} of ∓ 27 K, exactly the difference found for these four stars. The T_{eff} offset between our study and Carretta et al. can be explained by the stated uncertainties in the V -band zeropoints.

On average, our $\log g$ values are lower than those calculated by Carretta et al. (2014) by 0.21 ± 0.02 dex ($\sigma = 0.04$ dex). Small differences in the adopted solar constants, mass of stars on the RGB in NGC 4833, and distance modulus to NGC 4833 only affect this offset by 0.04 dex. Adopting the Carretta et al. T_{eff} values changes the $\log g$ values by only 0.01 dex. We adopt 0.21 dex as the systematic uncertainty in $\log g$.

Our v_t values are greater by 0.18 ± 0.04 km s $^{-1}$ ($\sigma = 0.08$ km s $^{-1}$) for the four stars in common with Carretta et al. (2014). We adopt 0.18 km s $^{-1}$ as the systematic uncertainty in v_t .

Our metallicities (derived from Fe I lines) are lower by 0.20 ± 0.02 dex ($\sigma = 0.04$ dex) for the four stars in common with Carretta et al. (2014). The stated offset accounts for the different adopted solar Fe abundances. The discrepancy can be attributed to the model atmosphere grids and line analysis codes, as we now show. We rederive metallicities for these four stars using the Carretta et al. model atmosphere parameters, their line list and equivalent widths, our adopted grid of models (ATLAS9), and our adopted line analysis code (MOOG). The metallicities are lower by 0.20 ± 0.01 dex ($\sigma = 0.02$ dex), which fully accounts for the discrepancy.

7 ABUNDANCE ANALYSIS

Abundances of lighter elements ($Z \leq 30$) that do not exhibit broad isotope shifts (IS) or hyperfine splitting structure (HFS) are derived from equivalent widths. We use MOOG to compute theoretical equivalent widths that are forced to match the measured values by adjusting the abundance. Abundances of all other elements are derived by matching synthetic spectra with the observed spectra. Lines of these elements are denoted by the word ‘‘synth’’ in Table 4. When a line is not detected, we derive a 3σ abundance upper limit using a version of the formula presented on p. 590 of Frebel et al. (2008a), which is derived from equation A8 of Bohlin et al. (1983). These lines are denoted by the word ‘‘limit’’ in Table 4.

The atomic data for all lines examined are presented in Table 4. References for the $\log gf$ values, IS, and HFS (when available) are also given in Table 4. We derive C abundances from the CH $A^2\Delta - X^2\Pi$ G band ($\approx 4290\text{--}4330$ Å) using a line list kindly provided by B. Plez (2007, private communication). We derive N abundances from the CN $B^2\Sigma - X^2\Sigma$ violet band ($\approx 3875\text{--}3885$ Å) using the line

list from Kurucz & Bell (1995) after setting the C abundance using the CH G band.

We assume local thermodynamic equilibrium (LTE) holds for the line-forming layers of the atmosphere for all species except for those described below. We adopt non-LTE corrections for Li I (Lind et al. 2009), O I (Fabbian et al. 2009), Na I (Lind et al. 2011), and K I (Takeda et al. 2002). We use the correction for the nearest point on the grid when the stellar parameters extend beyond the edges of the grids of pre-computed non-LTE corrections. These corrections are included in the abundances presented in Tables 5, 6, and 7. We include an additional 0.1 dex statistical uncertainty in our error estimates to account for uncertainties in the corrections. We do not detect the Li I 6707 Å line; corrections are based on the 3σ upper limits and range from +0.10 to +0.21 dex. The non-LTE corrections for each of the three high-excitation O I 7771, 7774, and 7775 Å triplet lines range from -0.05 to -0.08 dex. The non-LTE corrections for the Na I 5682, 5688, 6154, and 6160 Å lines range from -0.02 to -0.14 dex. The K I 7698 Å line is contaminated by an atmospheric O₂ line; fortunately, however, the K I 7664 Å line is not contaminated. Roederer et al. (2014) found that these two lines yield consistent abundances (to better than 0.02 dex) after non-LTE corrections are applied. The non-LTE corrections for the K I 7664 Å line range from -0.58 to -0.61 dex.

We apply one additional correction to the O abundance derived from the high-excitation O I triplet lines. The [O I] 6300 Å line is generally considered to be a reliable abundance indicator formed under conditions of LTE (Kiselman 2001), but the O I 7771, 7774, and 7775 Å lines are not. Both abundance indicators are detected in seven stars. After applying the non-LTE corrections for the O I triplet lines, these lines still yield abundances higher by $+0.40 \pm 0.05$ dex ($\sigma = 0.13$ dex) than the [O I] 6300 Å line. This offset between the O I and [O I] lines is comparable to those found by García Pérez et al. (2006) and Roederer et al. (2014) in other metal-poor giants. We apply a downward correction to all non-LTE-corrected O I triplet line abundances by 0.40 dex. We include an additional 0.05 dex uncertainty to account for the uncertainty in this correction.

8 RESULTS

Table 5 lists the abundances or upper limits derived from each line examined in each star. Table 6 lists the weighted mean abundances of each species examined in each star. We adopt the upper limit that provides the strongest constraint on the abundance when multiple lines of the same species are not detected. The complete versions of Tables 5 and 6 are available in the Supplementary Information available online. Table 7 lists the mean abundance ratios of all species examined in NGC 4833. These are computed using the formalism presented in McWilliam et al. (1995). The statistical uncertainty, $\sigma_{\text{statistical}}$, is given by equation A17 of McWilliam et al. This includes uncertainties in the equivalent width measurement or line profile fitting, $\log gf$ values, and any non-LTE corrections. The total uncertainty, σ_{total} , is given by equation A16 of McWilliam et al. This includes the statistical uncertainty and uncertainties in the model atmosphere parameters. We recommend that σ_{neutrals} for

Table 5. Abundances derived from individual lines

Star	Species	Wavelength (Å)	$\log \epsilon$	σ
2-185	Li I	6707.80	< 0.53	...
2-185	[O I]	6300.30	< 7.16	...
2-185	O I	7771.94	< 6.83	...
2-185	O I	7774.17	< 7.24	...
2-185	O I	7775.39	< 7.40	...
2-185	Na I	5682.63	4.51	0.20
2-185	Na I	5688.20	4.60	0.20
2-185	Na I	6160.75	4.74	0.21
2-185	Mg I	4702.99	5.38	0.32
2-185	Mg I	5528.40	5.60	0.29
2-185	Mg I	5711.09	5.53	0.15
⋮	⋮	⋮	⋮	⋮

Notes.— The full version of Table 5 is available in the Supplementary Information section online.

element A be added in quadrature with $\sigma_{\text{statistical}}$ for element B when computing the ratio [A/B] when B is derived from lines of the neutral species. We recommend a similar procedure, utilizing σ_{ions} instead of σ_{neutrals} , when element B is derived from lines of the ionized species. The adopted solar reference abundances are listed in Table 8.

Figures 5 and 6 illustrate abundance ratios as a function of T_{eff} . In most cases, no trends are found. Subtle trends may be present in cases where one of the elements in question is known to vary with evolutionary status. A small downward trend of [C/Fe] and a corresponding increase in [N/Fe] are found with decreasing T_{eff} . The Li upper limits get progressively lower with decreasing T_{eff} , which is simply a reflection of relatively constant equivalent width upper limits (from relatively constant S/N levels) applied to stars with decreasing T_{eff} . There are also subtle differences at the $\approx 1-2\sigma$ level ($\approx 0.10-0.15$ dex) in the mean [X/Fe] ratios between the warm ($T_{\text{eff}} > 4500$ K) and cool ($T_{\text{eff}} < 4500$ K) stars, where “X” represents Sc, V I and II, Zn, Nd, Ce, Sm, Eu, and Dy. We investigate these differences in detail in Sections 9.3 and 9.5.

Table 9 lists the variations in abundance ratios that result from changes in the model atmosphere parameters for one representative star with high S/N ratios, 4-1255. The final column of Table 9 lists the total variation, calculated by adding the four individual variations in quadrature.

8.1 Comparison of abundance ratios

Table 7 also lists the mean abundance ratios derived by Carretta et al. (2014) from their UVES spectra of stars in NGC 4833. In many cases the two sets of mean abundances are in reasonable (2σ) agreement. At first glance, several [X/Fe] ratios are not in agreement, where “X” represents O I, Si I, Ca I, Sc II, Ti I and II, V I, Cr II, Co I, Ni I, Zn I, and Nd II. Most of these differences can be explained by the sets of lines used, the $\log gf$ values, and the adopted solar abundances, as we now show.

Carretta et al. (2014) used the atomic data and solar reference abundances presented in Gratton et al. (2003). Their approach ensures a uniform abundance scale for the

Table 6. Mean abundances in each star

Star	Species	N_{lines}	$\log \epsilon$	$[X/\text{Fe}]^a$	$\sigma_{\text{statistical}}$	σ_{total}	σ_{neutrals}	σ_{ions}
2-185	Fe I	102	5.33	-2.17	0.06	0.14	0.00	0.00
2-185	Fe II	6	5.27	-2.23	0.07	0.10	0.00	0.00
2-185	Li I	1	< 0.53
2-185	C (CH)	1	5.62	-0.64	0.10	0.22	0.15	0.15
2-185	N (CN)	1	7.29	1.63	0.20	0.28	0.23	0.23
2-185	O I	4	< 6.83	0.31
2-185	Na I	3	4.61	0.55	0.12	0.17	0.13	0.17
2-185	Mg I	3	5.52	0.09	0.07	0.14	0.09	0.15
⋮	⋮	⋮	⋮	⋮	⋮	⋮	⋮	⋮

Notes.— The full version of Table 6 is available in the Supplementary Information section online.

^a $[\text{Fe}/\text{H}]$ is given for Fe I and Fe II

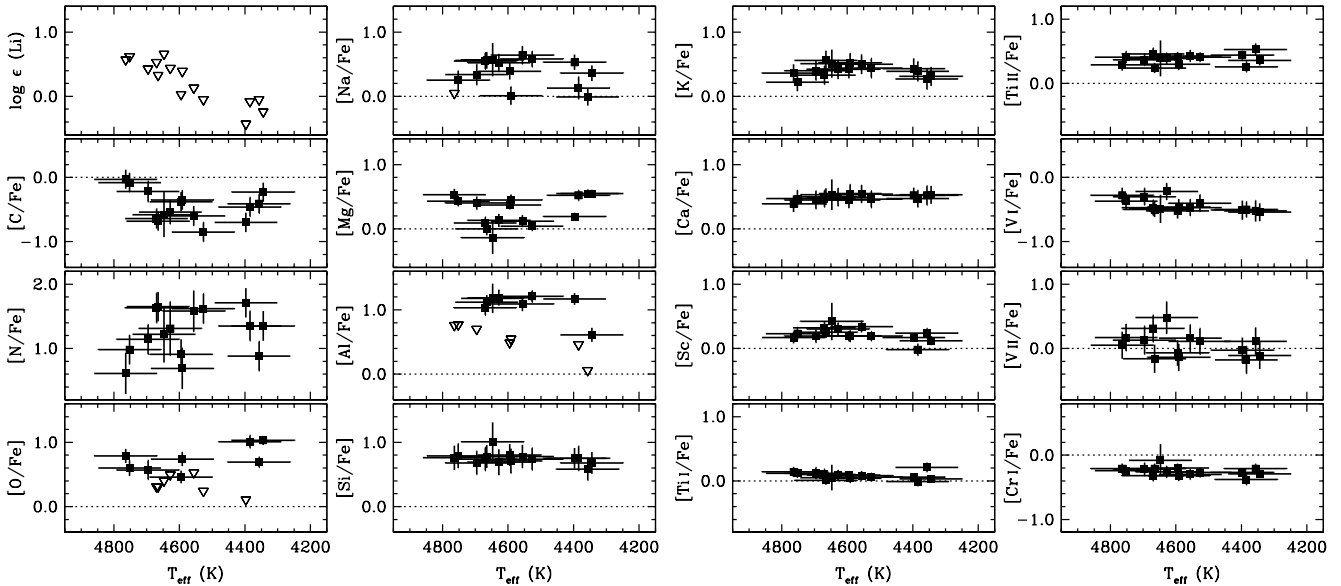


Figure 5. Derived $[X/\text{Fe}]$ ratios ($\log \epsilon$ for Li) as a function of T_{eff} for Li through Cr I. The dotted lines represent the solar ratios, and the downward facing triangles represent upper limits.

dozens of globular clusters observed in the last decade using GIRAFFE and UVES. Our analysis incorporates atomic data from more recent laboratory studies and adopts the Asplund et al. (2009) solar abundance scale. The appeal of using updated $\log gf$ values is that recent laboratory studies regularly report uncertainties on absolute transition probabilities as small as 5 per cent, which is effectively negligible when compared with other sources of uncertainty. The choice of $\log gf$ values is irrelevant if only relative differences are of interest and if the same set of lines is employed for each star. This condition is not met since the S/N and stellar parameters vary, thus we use updated $\log gf$ values whenever possible.

The $[\text{Ca}/\text{Fe}]$ ratios provide a good example of the consequences of this choice. There are seven Ca I lines studied in the GIRAFFE spectra obtained by Carretta et al. (2014). The Ca I $\log gf$ values used by Carretta et al. and those we adopt from NIST or Aldenius, Lundberg, & Blackwell-Whitehead (2009) differ

by -0.26 dex to $+0.27$ dex for these lines. Only one of these absolute differences is smaller than 0.17 dex. In our study, we use three of these lines and several others at shorter wavelengths. Thus the exact set of lines measured significantly affects the derived $[\text{Ca}/\text{Fe}]$ ratios. Substantial differences (≥ 0.05 dex) are also present in the adopted $\log gf$ values of lines of Na I, Si I, Sc II, Ti I, Fe II, and Ni I. It is impossible to assess the exact differences since no single source of $\log gf$ values covers all of the lines used by Carretta et al. and us.

Our use of the Asplund et al. (2009) solar abundance scale introduces several substantial differences in the $[X/\text{Fe}]$ ratios relative to Carretta et al. (2014). Our $[\text{O I}/\text{Fe}]$ ratios would change by -0.06 dex on their scale; $[\text{Na I}/\text{Fe}]$, $+0.07$ dex; $[\text{Mg I}/\text{Fe}]$, $+0.21$ dex; $[\text{Ca I}/\text{Fe}]$, $+0.11$ dex; $[\text{Ti II}/\text{Fe}]$, -0.13 dex; $[\text{Cr II}/\text{Fe}]$, -0.08 dex; $[\text{Mn I}/\text{Fe}]$, $+0.13$ dex; and $[\text{Zn I}/\text{Fe}]$, $+0.07$ dex.

We use our software, model atmospheres, and solar reference abundances to rederive the $[X/\text{Fe}]$ ratios using the

Table 7. Mean abundance ratios in NGC 4833

Ratio	Species or molecule	This study				Carretta et al. (2014)		
		Mean	Std. err.	Std. dev.	Num. stars	Notes	Mean	Std. err.
[C/Fe]	CH	-0.44	0.06	0.24	15	
[N/Fe]	CN	+1.28	0.09	0.36	15	
[O/Fe]	I	+0.81	0.08	0.22	8	1	+0.17	0.22
[Na/Fe]	I	+0.39	0.06	0.22	14	1	+0.52	0.29
[Mg/Fe]	I	+0.35	0.06	0.24	15		+0.27	0.22
[Al/Fe]	I	+1.09	0.07	0.20	8	1	+0.90	0.34
[Si/Fe]	I	+0.74	0.02	0.09	15		+0.47	0.04
[K/Fe]	I	+0.40	0.02	0.10	15	
[Ca/Fe]	I	+0.49	0.011	0.04	15		+0.35	0.01
[Sc/Fe]	II	+0.19	0.03	0.11	15		-0.11	0.01
[Ti/Fe]	I	+0.08	0.014	0.06	15		+0.18	0.02
[Ti/Fe]	II	+0.39	0.02	0.08	15		+0.23	0.01
[V/Fe]	I	-0.44	0.03	0.10	15		-0.08	0.01
[V/Fe]	II	+0.05	0.05	0.19	14	
[Cr/Fe]	I	-0.26	0.02	0.07	15		-0.24	0.02
[Cr/Fe]	II	+0.29	0.03	0.12	12		+0.01	0.05
[Mn/Fe]	I	-0.58	0.03	0.11	15		-0.54	0.01
[Fe/H]	I	-2.25	0.02	0.09	15		-2.02	0.01
[Fe/H]	II	-2.19	0.013	0.05	15		-2.01	0.02
[Co/Fe]	I	-0.39	0.04	0.14	14	1	-0.03	0.03
[Ni/Fe]	I	-0.06	0.015	0.06	15		-0.18	0.01
[Cu/Fe]	I	-0.65	0.05	0.14	9	1	-0.80	0.09
[Zn/Fe]	I	+0.19	0.02	0.10	15		+0.07	0.03
[Rb/Fe]	I	< +0.85	15	
[Sr/Fe]	II	+0.18	0.03	0.12	14	
[Y/Fe]	II	-0.22	0.03	0.11	15		-0.15	0.06
[Zr/Fe]	II	+0.25	0.03	0.11	14	
[Nb/Fe]	II	< +0.93	2	
[Mo/Fe]	I	+0.19	0.11	0.23	4	1
[Ba/Fe]	II	-0.02	0.016	0.06	15		-0.06	0.07
[La/Fe]	II	+0.08	0.03	0.13	14		+0.05	0.03
[Ce/Fe]	II	+0.03	0.03	0.11	15	
[Pr/Fe]	II	+0.19	0.09	0.29	10	1
[Nd/Fe]	II	+0.18	0.03	0.11	15	
[Sm/Fe]	II	+0.29	0.03	0.11	14	
[Eu/Fe]	II	+0.36	0.03	0.13	15	
[Gd/Fe]	II	+0.32	0.09	0.21	6	1
[Tb/Fe]	II	+0.19	0.04	0.05	2	1
[Dy/Fe]	II	+0.43	0.05	0.17	13	1
[Ho/Fe]	II	+0.16	0.18	0.18	1	1
[Er/Fe]	II	+0.33	0.08	0.20	7	1
[Tm/Fe]	II	+0.19	0.07	0.10	2	1
[Yb/Fe]	II	+0.01	0.08	0.25	9	1
[Hf/Fe]	II	+0.27	0.04	0.06	2	1
[Ir/Fe]	I	+0.66	0.11	0.11	1	1
[Pb/Fe]	I	< +0.02	15	
[Th/Fe]	II	< +0.32	14	

Notes— 1. Does not include one or more upper limits

Carretta et al. (2014) line lists and equivalent widths for the four stars in common. On our scale, the Carretta et al. ratios change by $+0.15 \pm 0.04$ dex for [O I/Fe], $+0.10 \pm 0.03$ dex for [Si I/Fe], -0.05 ± 0.05 dex for [Ca I/Fe], $+0.05 \pm 0.03$ dex for [Ti I/Fe], and $+0.07 \pm 0.03$ dex for [Ni I/Fe]. These account for about half of the total discrepancy in O I, Si I, and Ni I, but they widen the discrepancy for Ca I and Ti I. V I and Co I cannot be assessed due to the corrections for HFS. Carretta et al. only derived abundances for Ti II, Cr II,

Zn I, and Nd II from their UVES spectra, so we have no data in common.

To summarize, some mean [X/Fe] ratios we have derived are in disagreement with those found by Carretta et al. (2014). We can explain some of these discrepancies in part by the different solar reference abundances, and we attribute others to the different sets of lines used and the log *gf* values of those lines. Finally, the exact sets of stars observed could affect the mean values of the light elements known to vary star-by-star.

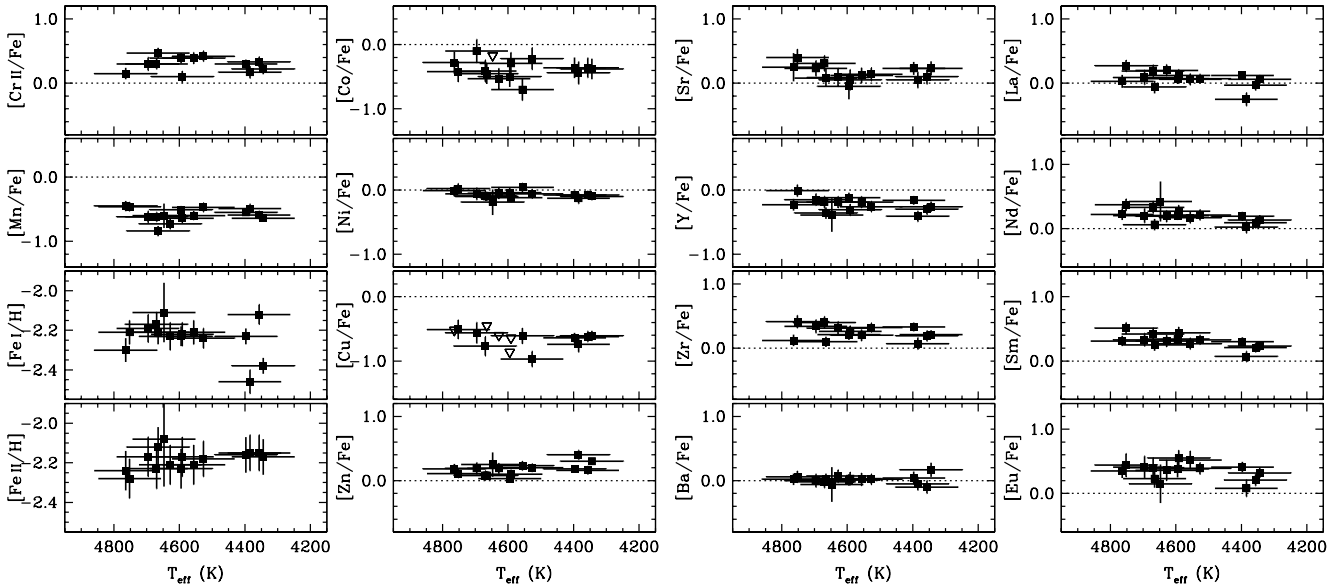


Figure 6. Derived $[X/Fe]$ ratios ($[Fe/H]$ for Fe) as a function of T_{eff} for Cr II through Yb. The dotted lines represent the solar ratios, and the downward facing triangles represent upper limits.

9 DISCUSSION

9.1 Iron

We derive a mean metallicity, $\langle [Fe/H] \rangle$, of -2.25 ± 0.02 ($\sigma = 0.09$) from Fe I lines in the 15 stars observed in NGC 4833. We derive $\langle [Fe/H] \rangle = -2.19 \pm 0.013$ ($\sigma = 0.05$) from Fe II lines. The standard deviation associated with each of these values does not exceed that expected from the model atmosphere uncertainties listed in Table 9. We find no evidence for an intrinsic dispersion in the Fe abundances from one star to another within NGC 4833, which reaffirms the results of Carretta et al. (2014).

As noted in Section 6.2, we find a metallicity lower by 0.20 ± 0.02 dex ($\sigma = 0.04$ dex) relative to Carretta et al. (2014) for four stars in common. We have identified the causes of this discrepancy previously, and now we compare the metallicity of NGC 4833 to an external metallicity standard. The temperature of the K-giant Arcturus (α Boo) is known to better than 30 K from measurements of its angular diameter and bolometric flux. Koch & McWilliam (2008) performed a differential abundance analysis between Arcturus and red giants in the moderately metal-poor globular cluster 47 Tuc ($[Fe/H] = -0.76 \pm 0.01$ [statistical] ± 0.04 [systematic]). Koch & McWilliam (2011) extended this differential analysis to the very metal-poor cluster NGC 6397 ($[Fe/H] = -2.10 \pm 0.02$ [statistical] ± 0.07 [systematic]), which we use for our comparison.

We use the Fe I line list from Koch & McWilliam (2011) to identify 19 lines in common to three red giants in NGC 6397 (stars 7230, 8958, and 13414) and three red giants in NGC 4833 (stars 3-742, 4-341, 4-1255) with similar T_{eff} . We measure equivalent widths for each of these lines in NGC 4833, and we perform a differential abundance analysis between NGC 6397 and NGC 4833. We find a mean difference in $[Fe/H]$ of $+0.09 \pm 0.04$ dex between NGC 6397 and NGC 4833. In other words, if we adopt $[Fe/H] = -2.10 \pm 0.02$ for NGC 6397 as derived by

Koch & McWilliam (2011), we infer $[Fe/H] = -2.19 \pm 0.04$ for NGC 4833. This value is in fair agreement with our derived mean metallicity, $[Fe/H] = -2.25 \pm 0.02$. On the basis of the differential globular cluster abundance scale established by Koch & McWilliam relative to Arcturus, we prefer the lower metallicity value for NGC 4833.

9.2 Lithium through Silicon

We do not detect Li in any of the stars in our sample. The upper limits we derive are illustrated in Figure 5. These limits rule out substantial enhancement of the surface Li abundances in these stars, as has been found in a few red giants in other globular clusters (e.g., Kraft et al. 1999; Smith, Shetrone, & Keane 1999).

Figure 7 shows the relationships among the light elements C, N, and Na in NGC 4833. There is a clear decrease in the $[C/Fe]$ ratio with increasing $[N/Fe]$. $[C/Fe]$ also anticorrelates with $[Na/Fe]$, and $[N/Fe]$ correlates with $[Na/Fe]$. There is no compelling evidence for a bi-modality in either $[C/Fe]$ or $[N/Fe]$, but this tentative conclusion should be checked using larger sample sizes.

Figure 8 reveals a prominent anti-correlation between $[O/Fe]$ and $[Na/Fe]$ in our sample of 15 stars in NGC 4833. Carretta et al. (2014) detected O and Na in 51 stars in their sample, and these data are shown for comparison in Figure 8. The offset between our mean $[O/Fe]$ and that of Carretta et al. is apparent. This offset is strongly influenced by two factors. First, we only derive upper limits for $[O/Fe]$ in stars with $[O/Fe] < +0.4$, while Carretta et al. detected O in ≈ 20 such stars. These upper limits are not included in the mean $[O/Fe]$ value reported in Table 7. Second, two of the eight stars with O detections in our sample show $[O/Fe] \approx +1.0$, which is ≈ 0.2 dex higher than the next-highest $[O/Fe]$ ratio in any other star in our sample. Neither of these stars, 4-224 and 4-1225, was included in the Carretta et al. sample. The remaining stars in our sample

Table 9. Variations in Abundance Ratios Resulting from Changes in the Model Atmosphere Parameters for Star 4-1255

Ratio	Ion	$\delta[X/Y]/\delta T_{\text{eff}}$	$\delta[X/Y]/\delta \log g$	$\delta[X/Y]/\delta v_t$	$\delta[X/Y]/\delta[M/H]$	$\sqrt{\Sigma \delta_i^2}$
[O/Fe]	I	-0.27	+0.10	+0.06	+0.04	0.30
[Na/Fe]	I	-0.06	+0.00	+0.07	+0.01	0.09
[Mg/Fe]	I	-0.06	-0.03	+0.01	+0.00	0.07
[Al/Fe]	I	-0.08	+0.01	+0.07	+0.01	0.11
[Si/Fe]	I	-0.11	+0.04	+0.07	+0.03	0.14
[K/Fe]	I	+0.03	+0.01	-0.03	-0.01	0.04
[Ca/Fe]	I	-0.01	+0.02	-0.03	-0.01	0.04
[Sc/Fe]	II	+0.01	+0.05	+0.07	+0.05	0.10
[Ti/Fe]	I	+0.08	-0.01	+0.02	-0.02	0.09
[Ti/Fe]	II	-0.06	-0.02	-0.04	-0.01	0.08
[V/Fe]	I	+0.11	+0.02	+0.07	+0.05	0.14
[V/Fe]	II	-0.02	-0.05	+0.00	-0.07	0.09
[Cr/Fe]	I	+0.04	-0.01	+0.02	-0.01	0.05
[Cr/Fe]	II	-0.12	+0.00	+0.03	-0.02	0.13
[Mn/Fe]	I	+0.03	+0.04	+0.10	+0.05	0.12
[Fe/H]	I	+0.15	-0.03	-0.07	-0.02	0.17
[Fe/H]	II	-0.06	+0.08	-0.04	+0.05	0.12
[Co/Fe]	I	+0.13	+0.00	+0.01	+0.02	0.13
[Ni/Fe]	I	-0.03	+0.02	+0.05	+0.01	0.06
[Cu/Fe]	I	-0.02	+0.03	+0.08	+0.02	0.09
[Zn/Fe]	I	-0.18	+0.07	+0.04	+0.05	0.20
[Sr/Fe]	II	+0.01	-0.06	+0.02	-0.07	0.09
[Y/Fe]	II	+0.09	-0.01	+0.02	+0.00	0.09
[Zr/Fe]	II	+0.05	-0.01	+0.02	+0.00	0.05
[Mo/Fe]	I	+0.03	+0.00	+0.05	-0.01	0.06
[Ba/Fe]	II	+0.16	-0.02	-0.08	+0.00	0.18
[La/Fe]	II	+0.10	-0.02	+0.05	+0.01	0.11
[Ce/Fe]	II	+0.07	+0.00	+0.05	+0.02	0.09
[Pr/Fe]	II	+0.13	+0.02	+0.08	+0.03	0.16
[Nd/Fe]	II	+0.13	+0.00	+0.04	+0.02	0.14
[Sm/Fe]	II	+0.11	-0.01	+0.03	+0.03	0.12
[Eu/Fe]	II	+0.09	+0.02	+0.07	+0.01	0.12
[Gd/Fe]	II	+0.09	+0.05	+0.04	-0.01	0.11
[Tb/Fe]	II	+0.10	+0.03	+0.07	+0.05	0.14
[Dy/Fe]	II	+0.07	-0.02	-0.02	-0.02	0.08
[Er/Fe]	II	+0.00	+0.03	+0.00	+0.01	0.03
[Tm/Fe]	II	+0.09	-0.04	+0.00	-0.08	0.13
[Yb/Fe]	II	+0.21	-0.09	+0.04	-0.08	0.25
[Hf/Fe]	II	+0.12	+0.07	+0.09	-0.02	0.17

Notes— $\delta T_{\text{eff}} = +97$ K, $\delta \log g = +0.21$ dex, $\delta v_t = +0.18$ km s⁻¹, $\delta[M/H] = +0.20$; see Sections 6.1 and 6.2 for details.

are found to overlap the Carretta et al. data relatively well in the [O/Fe] versus [Na/Fe] plane.

Our data and that of Carretta et al. (2014) independently exhibit a broad anti-correlation between [O/Fe] and [Na/Fe]. This includes stars with [O/Fe] and [Na/Fe] ratios consistent with normal halo field stars and stars with depleted [O/Fe] and enhanced [Na/Fe] ratios. Carretta et al. calculated that 31 ± 8 per cent of stars in NGC 4833 belong to the primordial component (i.e., those with normal [O/Fe] and [Na/Fe] ratios). Another 59 ± 11 per cent of stars belong to the intermediate component (i.e., those with depleted [O/Fe] ratios and enhanced [Na/Fe] ratios), and 10 ± 4 per cent of stars belong to the extreme component (i.e., those with $[O/Na] < -0.9$; Carretta et al. 2009a). Our sample is more than three times smaller than that of Carretta et al., so we do not attempt to rederive these fractions. The fraction of stars in the primordial component, one-third, is typical of most globular clusters that have been studied. The

fraction of stars in the extreme component is larger than in most clusters, which have typically 2–3 per cent or less (Carretta et al. 2009a).

Figure 8 also reveals correlations between [O/Fe] and [Mg/Fe], [Na/Fe] and [Al/Fe], possibly [Na/Fe] and [Si/Fe], and possibly [Al/Fe] and [Si/Fe]. Anti-correlations are also present among [O/Fe] and [Al/Fe], [Na/Fe] and [Mg/Fe], and [Mg/Fe] and [Al/Fe]. These features were also present in the sample of Carretta et al. (2014). Collectively, these abundance patterns indicate that proton-capture reactions operating at high temperatures occurred in the stars that enriched some of the present-day members of NGC 4833.

Carretta et al. (2014) identified a bi-modal distribution among the Mg and Al abundances derived from the UVES spectra. Our data confirm this separation, which is easily discerned in the [O/Fe] versus [Al/Fe], [Na/Fe] versus [Mg/Fe], [Na/Fe] versus [Al/Fe], and [Mg/Fe] versus [Al/Fe] planes in Figure 8.

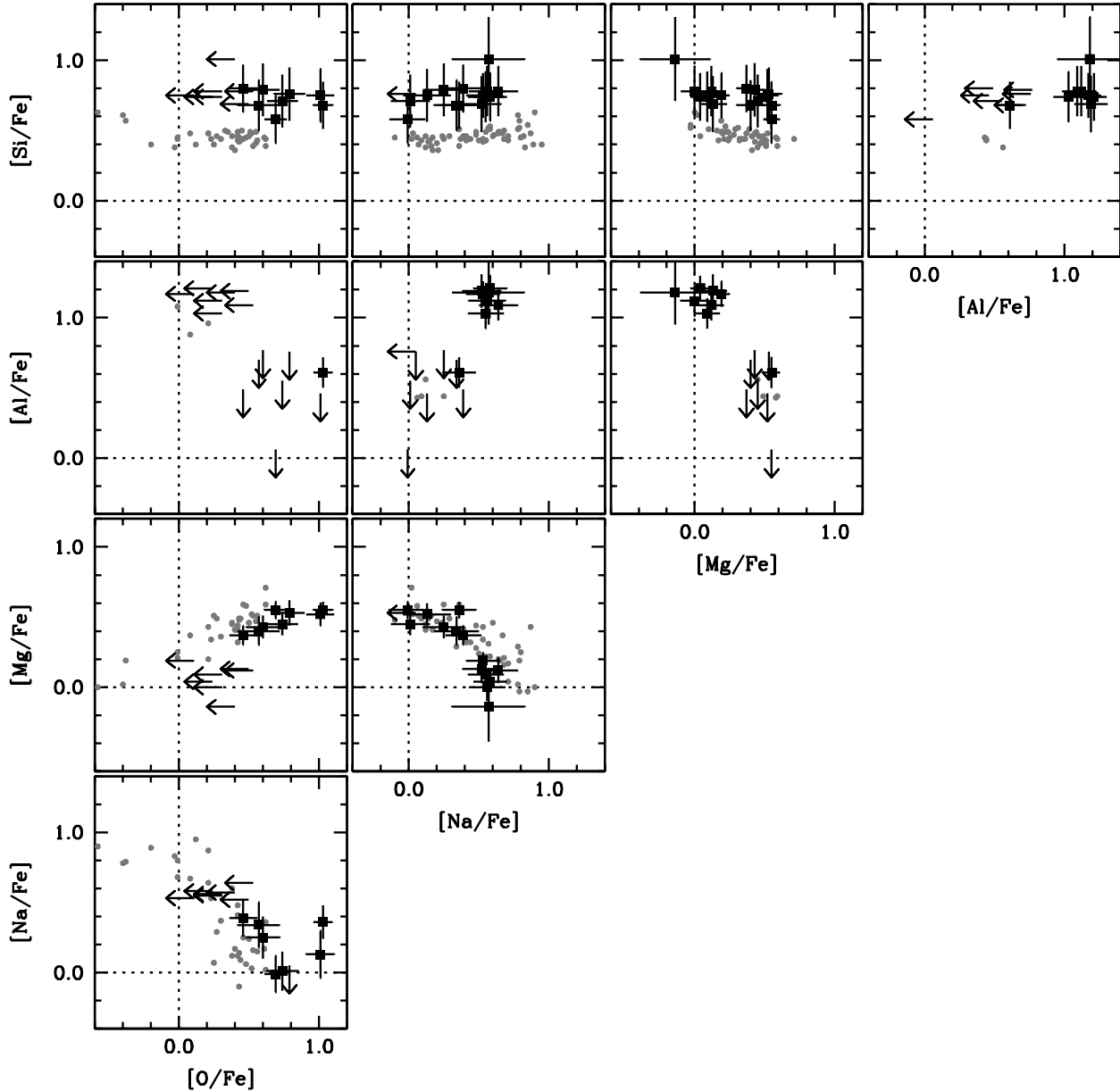


Figure 8. Relationships among O, Na, Mg, Al, and Si in NGC 4833. Black symbols mark data from this study, and small gray circles mark data from Carretta et al. (2014). The dotted lines indicate the solar ratios.

Trends involving $[\text{Si}/\text{Fe}]$ are more subtle. Carretta et al. found evidence of such trends in their sample, which can be seen by simple inspection of their Figure 8. Similar inspection of our Figure 8 only hints that $[\text{Si}/\text{Fe}]$ may correlate with $[\text{Na}/\text{Fe}]$ and $[\text{Al}/\text{Fe}]$ and anti-correlate with $[\text{Mg}/\text{Fe}]$. We divide our sample into two groups to test whether these correlations are significant. The $[\text{Mg}/\text{Fe}]$ ratios are well-separated into two groups divided at $[\text{Mg}/\text{Fe}] \approx +0.3$, and we compute the weighted mean $[\text{Si}/\text{Fe}]$ ratio within each group. In the Mg-rich group of stars, $\langle [\text{Si}/\text{Fe}] \rangle = +0.72 \pm 0.03$; in the Mg-poor group, $\langle [\text{Si}/\text{Fe}] \rangle = +0.76 \pm 0.04$. The $[\text{Si}/\text{Fe}]$ ratios are not significantly different in the Mg-rich and Mg-poor groups of stars.

We also compute p -values for the linear correlation coefficient r between $[\text{Si}/\text{Fe}]$ and other light-element ratios. The

p -value gives the probability that a random sample of N uncorrelated points would yield an experimentally-derived value $\geq |r|$. For example, the p -value for the $[\text{Na}/\text{Fe}]$ and $[\text{Mg}/\text{Fe}]$ ratios shown in Figure 8 is 0.0002. The p -values between $[\text{Si}/\text{Fe}]$ and $[\text{O}/\text{Fe}]$, $[\text{Na}/\text{Fe}]$, $[\text{Mg}/\text{Fe}]$, and $[\text{Al}/\text{Fe}]$ are 0.645, 0.077, 0.019, and 0.356, respectively. Only the anti-correlation between $[\text{Mg}/\text{Fe}]$ and $[\text{Si}/\text{Fe}]$ is significant at the 2σ level in our data.

Censored (“survivor”) statistical tests can be applied to check whether the $[\text{Si}/\text{Fe}]$ correlations may be significant if upper limits are included. We apply the generalized version of Kendall’s τ rank correlation test to our data using the ASURV code (Rev. 1; Lavalley, Isobe, & Feigelson 1992) as described in Isobe, Feigelson, & Nelson (1986). This test evaluates whether a correlation may be present between two

Table 8. Adopted solar abundances

Element	Z	$\log \epsilon_{\odot}$	Photospheric (P) or meteoritic (M)
C	6	8.43	P
N	7	7.83	P
O	8	8.69	P
Na	11	6.24	P
Mg	12	7.60	P
Al	13	6.45	P
Si	14	7.51	P
K	19	5.03	P
Ca	20	6.34	P
Sc	21	3.15	P
Ti	22	4.95	P
V	23	3.93	P
Cr	24	5.64	P
Mn	25	5.43	P
Fe	26	7.50	P
Co	27	4.99	P
Ni	28	6.22	P
Cu	29	4.19	P
Zn	30	4.56	P
Rb	37	2.52	P
Sr	38	2.87	P
Y	39	2.21	P
Zr	40	2.58	P
Nb	41	1.46	P
Mo	42	1.88	P
Ba	56	2.18	P
La	57	1.10	P
Ce	58	1.58	P
Pr	59	0.72	P
Nd	60	1.42	P
Sm	62	0.96	P
Eu	63	0.52	P
Gd	64	1.07	P
Tb	65	0.30	P
Dy	66	1.10	P
Ho	67	0.48	P
Er	68	0.92	P
Tm	69	0.10	P
Yb	70	0.92	M
Hf	72	0.85	P
Ir	77	1.38	P
Pb	82	2.04	M
Th	90	0.06	M

variables when upper limits are found in either variable. We find that correlations among $[\text{Na}/\text{Fe}]$, $[\text{Mg}/\text{Fe}]$, and $[\text{Al}/\text{Fe}]$ are all highly significant ($p < 0.004$ in each case). We also find that $[\text{Si}/\text{Fe}]$ does not exhibit a significant correlation with either $[\text{Na}/\text{Fe}]$ or $[\text{Al}/\text{Fe}]$ if the upper limits are considered ($p > 0.12$ in each case).

We are unable to reproduce correlations between $[\text{Si}/\text{Fe}]$ and any other ratios, except perhaps $[\text{Mg}/\text{Fe}]$, in our data. Our sample size is considerably smaller than that of Carretta et al. (2014), which may explain the difference in our results.

9.3 Potassium through Zinc

Figure 9 illustrates the relationships among $[\text{Mg}/\text{Fe}]$, $[\text{K}/\text{Fe}]$, $[\text{Ca}/\text{Fe}]$, and $[\text{Sc}/\text{Fe}]$. Visual inspection of Figure 9 suggests

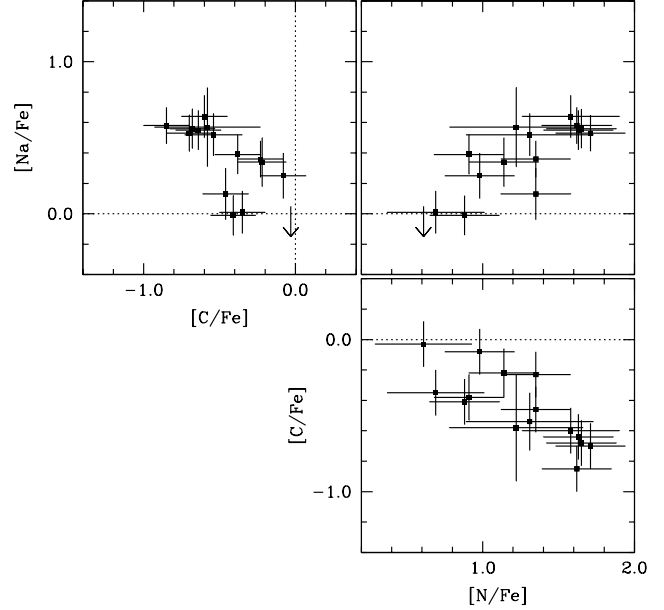


Figure 7. Relationships among C, N, and Na in NGC 4833. Black symbols mark data from this study. The dotted lines indicate the solar ratios.

that $[\text{K}/\text{Fe}]$ might anti-correlate with $[\text{Mg}/\text{Fe}]$. We calculate the mean $[\text{K}/\text{Fe}]$ ratios in the Mg-rich and Mg-poor groups of stars. We find $\langle [\text{K}/\text{Fe}] \rangle = +0.36 \pm 0.03$ for the Mg-rich group. We find $\langle [\text{K}/\text{Fe}] \rangle = +0.45 \pm 0.03$ for the Mg-poor group. These ratios are only distinct at the $\sim 1.5\sigma$ level, which is not significant. The p -value for the linear correlation between $[\text{Mg}/\text{Fe}]$ and $[\text{K}/\text{Fe}]$ is 0.018, which is significant. If $[\text{Mg}/\text{Fe}]$ and $[\text{K}/\text{Fe}]$ are anti-correlated, we might also expect correlations between $[\text{K}/\text{Fe}]$ and $[\text{Na}/\text{Fe}]$, $[\text{Al}/\text{Fe}]$, or $[\text{Si}/\text{Fe}]$; however, the p -values for the correlations between $[\text{K}/\text{Fe}]$ and other light elements are not significant at the 2σ level. We conclude that the evidence for an anti-correlation between $[\text{Mg}/\text{Fe}]$ and $[\text{K}/\text{Fe}]$ is curious but not compelling.

Hints of an anti-correlation between $[\text{Mg}/\text{Fe}]$ and $[\text{Sc}/\text{Fe}]$ are seen in Figure 9, but a closer analysis suggests otherwise. Figure 5 demonstrates that the three lowest $[\text{Sc}/\text{Fe}]$ ratios are found in three of the four coolest stars in our sample, signaling that these low ratios could be an artifact of the analysis. This correlation appears weaker if only the 11 stars with $T_{\text{eff}} > 4500$ K are considered. When dividing the sample of all 15 stars into Mg-rich and Mg-poor groups, we find $\langle [\text{Sc}/\text{Fe}] \rangle = +0.16 \pm 0.03$ in the Mg-rich group and $\langle [\text{Sc}/\text{Fe}] \rangle = +0.25 \pm 0.04$ in the Mg-poor group. If only the 11 stars with $T_{\text{eff}} > 4500$ K are considered, we find $\langle [\text{Sc}/\text{Fe}] \rangle = +0.19 \pm 0.01$ in the Mg-rich group and $\langle [\text{Sc}/\text{Fe}] \rangle = +0.27 \pm 0.04$ in the Mg-poor group. The $[\text{Sc}/\text{Fe}]$ ratios are not distinct at the 2σ level. We also conduct a line-by-line differential analysis of the $[\text{Sc}/\text{Fe}]$ ratios in two stars (2-185 and 2-918) with similar stellar parameters ($T_{\text{eff}} = 4670$ K and 4696 K, respectively) and different $[\text{Mg}/\text{Fe}]$ ratios ($[\text{Mg}/\text{Fe}] = +0.09$ and $+0.40$, respectively). An unweighted average of these differentials yields $\delta[\text{Sc}/\text{Fe}] = +0.018 \pm 0.043$ dex, which indicates no difference. Finally, we note that Carretta et al. (2014) found no evidence for an anti-correlation between $[\text{Mg}/\text{Fe}]$ and $[\text{Sc}/\text{Fe}]$ in their data, which are also shown in Figure 8. We conclude

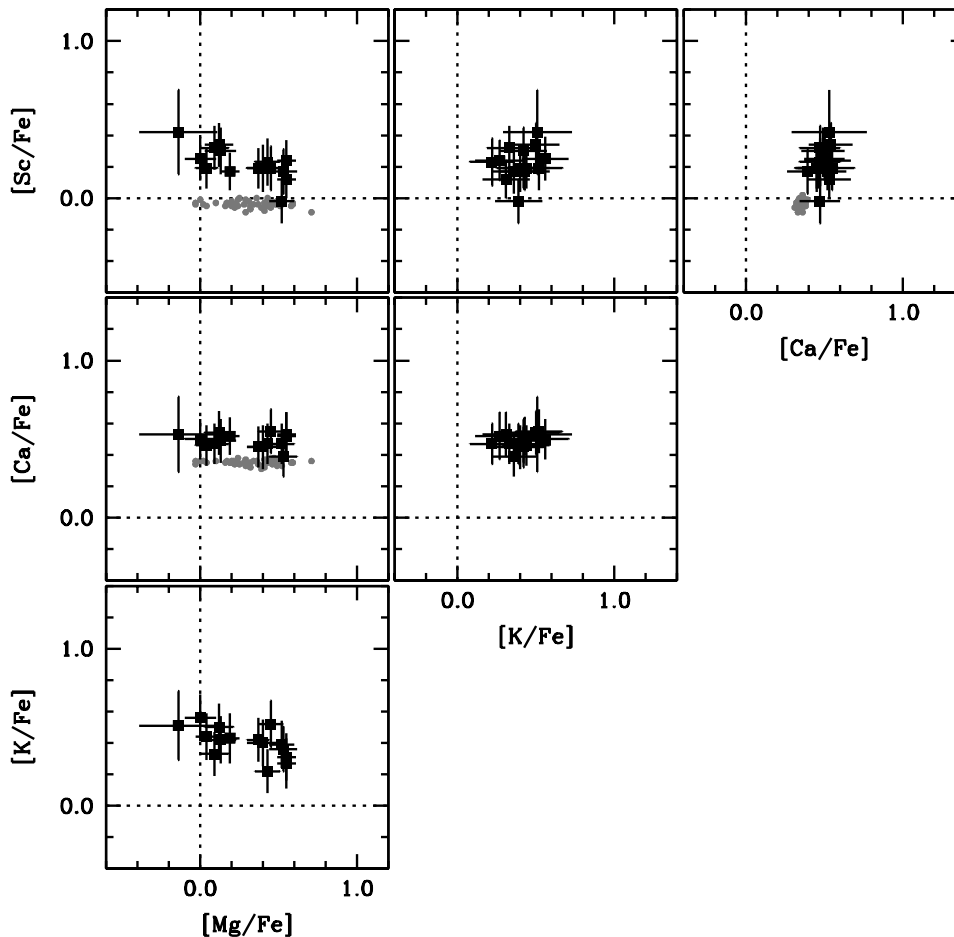


Figure 9. Relationships among Mg, K, Ca, and Sc in NGC 4833. Black symbols mark data from this study, and small gray circles mark data from Carretta et al. (2014). The dotted lines indicate the solar ratios.

that there is no compelling evidence for variations in the [Sc/Fe] ratios within NGC 4833.

Cohen, Huang, & Kirby (2011), Cohen & Kirby (2012), and Mucciarelli et al. (2012) detected an anti-correlation between [Mg/Fe] and [K/Fe] in the massive, metal-poor globular cluster NGC 2419. Mucciarelli et al. (2015) found a smaller, but significant, anti-correlation between [Mg/Fe] and [K/Fe] in NGC 2808. These two massive clusters are the only ones where such relations have been identified (Carretta et al. 2013). Our results indicate that such extreme variations in K do not occur in NGC 4833. Cohen & Kirby (2012) also detected an anti-correlation between [Mg/Fe] and [Sc/Fe] in their NGC 2419 data, and there is no compelling evidence for a similar relation in NGC 4833.

Figure 10 compares the mean [X/Fe] ratios for elements in and near the iron group (loosely considered here as K through Zn; $19 \leq Z \leq 30$) in NGC 4833 and normal metal-poor halo field stars. The comparison stars are drawn from the sample of 98 red giants examined by Roederer et al. (2014). Upper limits in the comparison sample have been omitted from Figure 10 for clarity. Overall, there is excellent agreement between the mean [X/Fe] ratios for elements in the iron group in NGC 4833 and normal halo field stars.

Gratton, Sneden, & Carretta (2004) pointed out that

the [Ca/Fe] in two stars in NGC 4833 reported by Gratton & Ortolani (1989) is higher by ≈ 0.2 – 0.3 dex than the [Ca/Fe] ratio in other metal-poor globular clusters. The Gratton & Ortolani result was already at odds with the data of Pilachowski et al. (1983). Neither Carretta et al. (2014) nor we reproduce this high [Ca/Fe] ratio in NGC 4833.

9.4 Neutron-capture elements

Figure 11 illustrates the heavy-element abundance distributions in each star observed in NGC 4833. For comparison, Figure 11 also shows the abundance distribution of the main component of the r -process as found in the metal-poor giant CS 22892–052 (Sneden et al. 2003, 2009; Roederer et al. 2009). There is generally good agreement among the heavy-element abundance distribution from one star to the next in NGC 4833. Large variations in the heavy-element distributions, like those found in ω Cen (e.g., Norris & Da Costa 1995; Smith et al. 2000), M2 (Yong et al. 2014), M22 (Marino et al. 2009; Roederer et al. 2011), or NGC 1851 (Yong & Grundahl 2008; Carretta et al. 2011) are excluded.

Figure 12 shows the mean heavy element abundance distribution for all 15 stars observed in NGC 4833. Three templates are shown for comparison. The red line marks the main component of the r -process, and this line is identi-

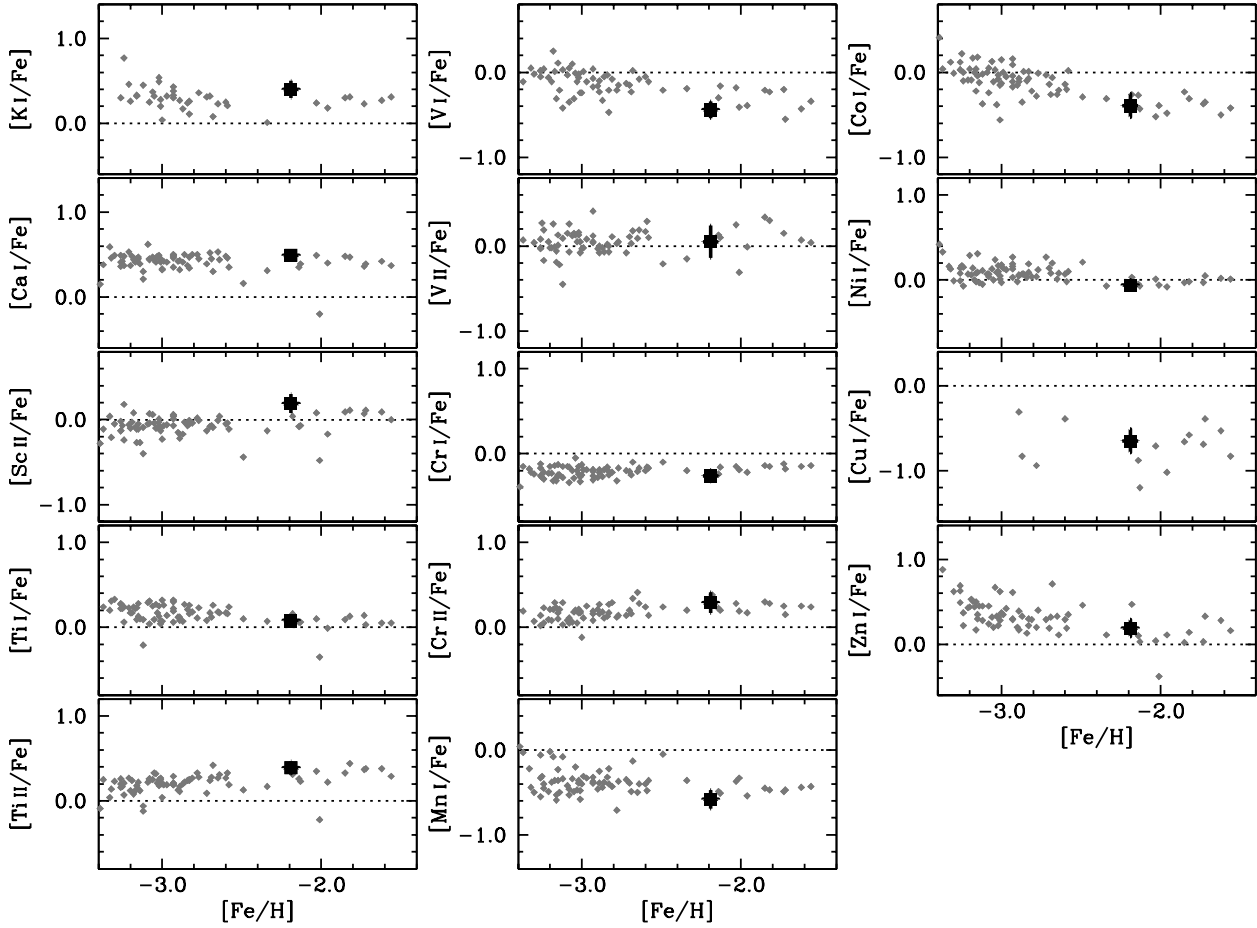


Figure 10. $[X/Fe]$ ratios for elements, X , in the iron group. The large black square indicates the mean abundances in NGC 4833, and the small gray diamonds represent individual red giant halo field stars analyzed by Roederer et al. (2014). The dotted lines indicate the solar ratios.

cal to that found in Figure 11. The thick gold line marks the distribution found in the metal-poor giant HD 122563 (Honda et al. 2006; Roederer et al. 2012), frequently referred to as the distribution produced by the weak component of the r -process. The long-dashed blue line marks the distribution predicted by the main and strong components of the s -process (Snedden, Cowan, & Gallino 2008; Bisterzo et al. 2011). These curves illustrate the general characteristics of r - and s -process nucleosynthesis and are not intended to be rigid representations. For example, the abundance distributions that result from s -process nucleosynthesis depend on the parameters of stars passing through the thermally-pulsing asymptotic giant branch phase of evolution (e.g., Busso, Gallino, & Wasserburg 1999; Bisterzo et al. 2010). The mean heavy element abundance distribution in NGC 4833 traces the main component of the r -process within $\approx 2\sigma$ for the elements with $Z \geq 57$. Ba ($Z = 56$) is enhanced by ≈ 0.3 dex relative to the template for the main component of the r -process when normalized to Eu. Sr, Y, Zr, and Mo ($Z = 38, 39, 40$, and 42 , respectively) are enhanced by $\approx 0.9, 0.5, 0.9$, and 0.6 dex.

One possible explanation of the Sr, Y, Zr, Mo, and Ba enhancements could be a small contribution from some form of s -process nucleosynthesis. If so, the results of Roederer et al. (2010) suggest that we might expect en-

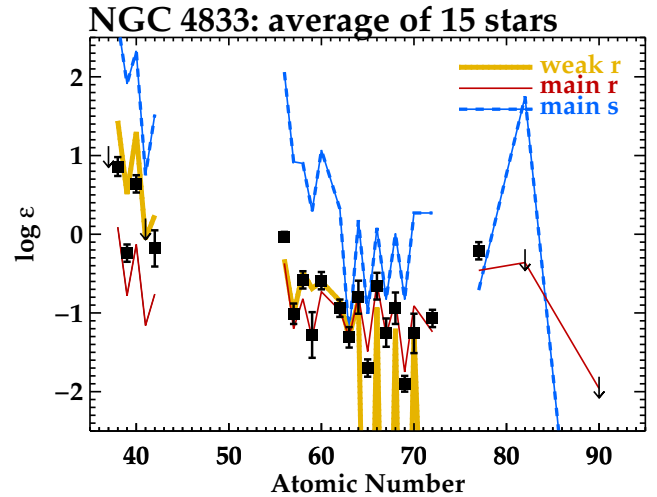


Figure 12. Average heavy element abundance pattern in NGC 4833. Filled squares mark detections, and arrows mark 3σ upper limits. The red line, thick gold line, and long-dashed blue line represent the main component of the r -process, the weak component of the r -process, and the main and strong components of the s -process as described in the text. Each of the three curves has been renormalized to the mean Eu abundance in NGC 4833.

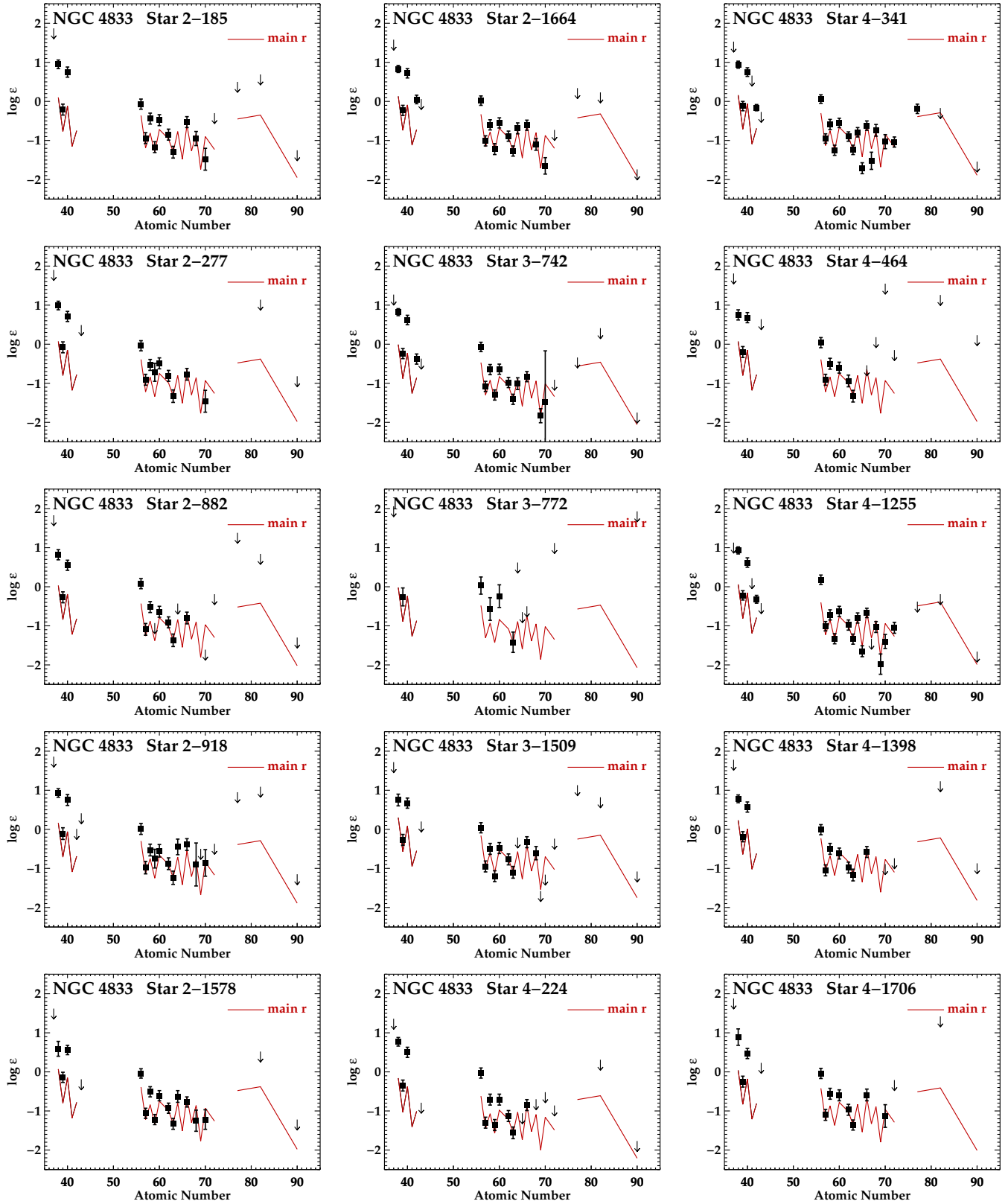


Figure 11. Heavy element abundance pattern for each star observed in NGC 4833. The red lines mark the template of the main component of the r -process (CS 22892–052). Filled symbols mark detections, and downward-facing triangles mark 3σ upper limits.

hancement of other elements with a substantial *s*-process component in solar system material, such as Yb, Hf, and Pb ($Z = 70, 72,$ and 82). No such enhancements are observed. Another possible explanation is that the weak component of the *r*-process has contributed to the heavy elements in NGC 4833. Halo field stars, like HD 122563, whose heavy elements have been produced by this mechanism do not typically show Ir ($Z = 77$), which is detected in NGC 4833. Our data suggest that the most likely explanation for the heavy element abundance distribution in NGC 4833 is a combination of the main and weak components of the *r*-process. A single *r*-process with physical characteristics intermediate between those of the main and weak components of the *r*-process could also be responsible.

Figure 13 compares the heavy element abundance distribution in NGC 4833 with six other metal-poor globular clusters. These clusters are selected for comparison because large numbers of heavy elements have been studied in multiple red giants within each cluster. The top panel of Figure 13 compares NGC 4833 with three clusters with $\langle[\text{Fe}/\text{H}]\rangle < -2.0$: M15 ($\langle[\text{Fe}/\text{H}]\rangle = -2.53$, RGB stars only; Sobeck et al. 2011), M92 ($\langle[\text{Fe}/\text{H}]\rangle = -2.70$; Roederer & Sneden 2011), and NGC 2419 ($\langle[\text{Fe}/\text{H}]\rangle = -2.06$; Cohen et al. 2011). The bottom panel of Figure 13 compares NGC 4833 with three other clusters with $\langle[\text{Fe}/\text{H}]\rangle > -2.0$: M2 ($\langle[\text{Fe}/\text{H}]\rangle = -1.68$, *r*-only group of stars; Yong et al. 2014), M5 ($\langle[\text{Fe}/\text{H}]\rangle = -1.40$, RGB stars only; Lai et al. 2011), and M22 ($\langle[\text{Fe}/\text{H}]\rangle = -1.81$, *r*-only group of stars; Roederer et al. 2011). The distributions are normalized to the Eu abundance to eliminate differences in the overall amount of heavy elements from one cluster to another. Regardless, these differences are small: $\langle[\text{Eu}/\text{Fe}]\rangle = +0.36$ (NGC 4833), $+0.55$ (M15), $+0.54$ (M92), $+0.38$ (M2), $+0.46$ (M5), $+0.35$ (M22), and $+0.30$ (NGC 2419).

A few general trends emerge from this comparison. First, the $[\text{X}/\text{Eu}]$ ratios are consistently sub-solar when “X” represents the lighter *n*-capture elements. The $[\text{Y}/\text{Eu}]$ and $[\text{Zr}/\text{Eu}]$ ratios are similar in all of the clusters where they have been examined. Small enhancements in Sr, Y, Zr, Mo, and Ba relative to the main component of the *r*-process are not unusual in metal-poor globular clusters. Second, there is a consistent upward trend in the $[\text{X}/\text{Eu}]$ ratios when “X” represents Ba through Sm. Third, there is a consistent downward trend in $[\text{X}/\text{Eu}]$ when “X” represents Gd through Yb. In summary, the heavy element distribution in NGC 4833 closely resembles that in other well-studied metal-poor globular clusters.

9.5 Heavy Element Dispersion in NGC 4833

In many globular clusters, the heavy elements appear to be homogeneous at the limit of observations. M15 is unique among all known clusters in that (1) it has a large range (spanning > 0.7 dex, Sneden et al. 1997; Worley et al. 2013) of heavy-element abundances relative to Fe, (2) the star-to-star abundance distribution remains relatively constant and appears to have originated predominantly via *r*-process nucleosynthesis, and (3) the heavy-element dispersion shows no correlation with the light element dispersion. These characteristics of M15 have been verified by Sneden et al. (1997, 2000), Preston et al. (2006), Otsuki et al. (2006), Sobeck et al. (2011), and Worley et al. (2013).

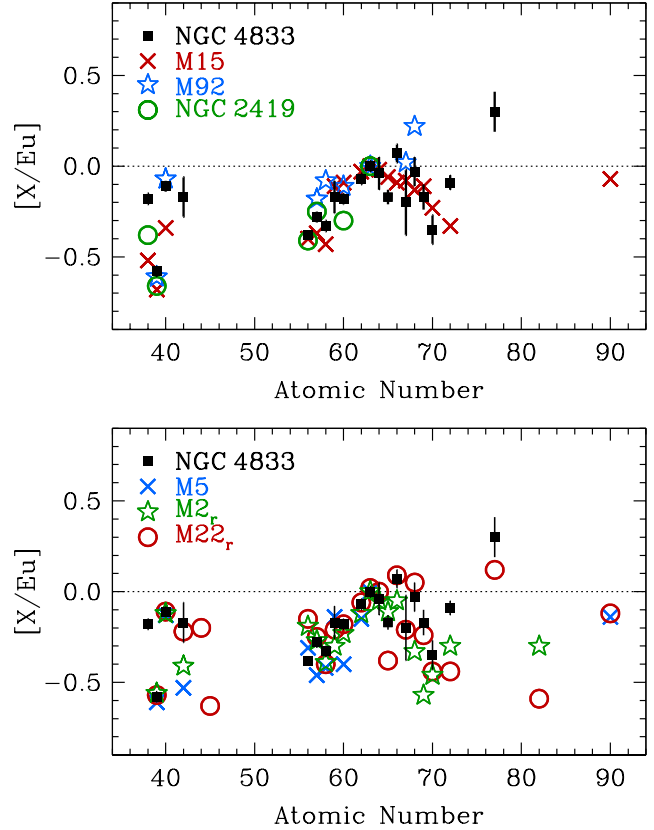


Figure 13. Average heavy element abundance pattern in NGC 4833 and six other metal-poor globular clusters. All ratios have been normalized to Eu. The three comparison clusters shown in the top panel have $\langle[\text{Fe}/\text{H}]\rangle < -2.0$, and the three comparison clusters shown in the bottom panel have $\langle[\text{Fe}/\text{H}]\rangle > -2.0$. References are given in the text.

Roederer (2011) reanalyzed literature data and presented evidence that several other metal-poor clusters (M3, M5, M13, and NGC 3201) may also exhibit a less-extreme *r*-process dispersion. Roederer & Sneden (2011) reported an *r*-process dispersion in M92, which was not found in the higher-quality data obtained by Cohen (2011). The $[\text{La}/\text{Fe}]$ and $[\text{Eu}/\text{Fe}]$ ratios showed a high degree of correlation for stars within each of these clusters. This would not be expected if the La and Eu abundances were independent measures of a sample with no cosmic dispersion in La or Eu. The $[\text{La}/\text{Eu}]$ ratios were constant, indicating that the distributions were constant and only the total amount of material (relative to, e.g., H or Fe) was changing. In principle, errors in the choice of model atmosphere could also produce the observed correlation since the La II and Eu II lines form similarly. This possibility was dismissed because no correlation was found among other species that might also form similarly, including Sc II and Ti II. In these clusters, the *r*-process dispersion did not correlate with the $[\text{Na}/\text{Fe}]$ ratio, which was chosen to represent the light-element dispersion commonly found in globular clusters.

We calculate a *p*-value of 0.001 for the relation between $[\text{La}/\text{Fe}]$ and $[\text{Eu}/\text{Fe}]$ in 15 stars in NGC 4833. The null hypothesis that $[\text{La}/\text{Fe}]$ and $[\text{Eu}/\text{Fe}]$ are not correlated is rejected at a $> 3\sigma$ significance level. Figure 14 illustrates the correlations between $[\text{Eu}/\text{Fe}]$ and eight heavy-element abun-

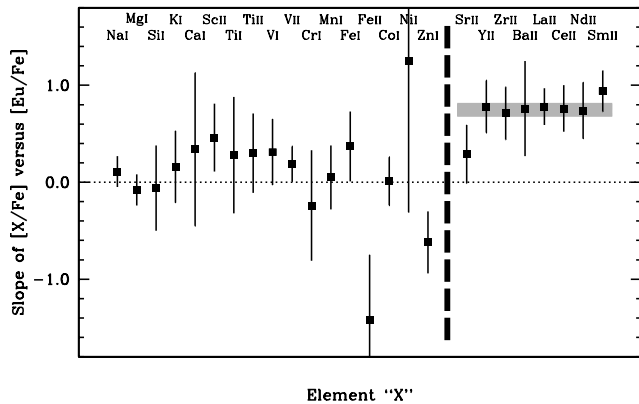


Figure 15. Slopes in the $[X/Fe]$ versus $[Eu/Fe]$ relationships, where “X” represents a given species. Recall that all ratios are constructed using ions with ions (e.g., $[La\ II/Fe\ II]$) and neutrals with neutrals (e.g., $[Na\ I/Fe\ I]$). The vertical dashed line separates the light from the heavy elements. The shaded region represents the mean $\pm 1\sigma$ of the slopes of the eight heavy elements shown to the right of the vertical dashed line. The horizontal dotted line marks a slope of zero.

dance ratios in NGC 4833. These eight pairs of ratios are selected because they have been measured in 14 or 15 of the 15 stars studied. The correlations bear strong resemblance to those identified by Roederer (2011). Of these eight ratios, only $[Sr/Fe]$, $[Ba/Fe]$, and $[Nd/Fe]$ do not correlate with $[Eu/Fe]$ at a $> 2\sigma$ level.

Weighted linear least-squares fits to the data are also shown in each panel in Figure 14. A slope of +1 corresponds to a direct correlation, -1 corresponds to a direct anti-correlation, and 0 corresponds to no correlation. The values of the slopes and 1σ uncertainties are illustrated in Figure 15. The slopes are remarkably consistent and non-zero, and the mean slope (0.75 ± 0.07 , $\sigma = 0.19$) is illustrated by the shaded box in Figure 15. Only the slope between $[Eu/Fe]$ and $[Sr/Fe]$ is not strongly positive among the elements produced by n -capture reactions.

Slopes of the relations between $[Eu/Fe]$ and lighter element ratios ($Z \leq 30$) are shown in Figure 15 for comparison. Most of these slopes are consistent with zero, in contrast to the slopes between $[Eu/Fe]$ and other elements produced by n -capture reactions. There is no coherent, significant pattern among them. This suggests that none of the lighter elements correlate with Eu or other n -capture elements.

Figure 16 illustrates $[Na/Fe]$ and eight of the heavy-element ratios shown in Figure 14. No correlations are apparent, and the p -values indicate that none of these correlations (including $[Na/Fe]$ versus $[Sm/Fe]$, not shown) is even 1σ significant. The heavy element dispersion is not related to the light element dispersion.

We have shown that the abundances of the n -capture elements in NGC 4833 correlate closely with one another but not the lighter elements. Next, we examine whether these correlations reflect true abundance dispersions or are an artifact of our analysis. Atoms in the same state (e.g., ions) would respond similarly to an inappropriate model atmosphere, and the resulting abundance distributions would be smeared out to lower and higher ratios in a correlated fashion. Table 9 lists the 1σ uncertainty in each $[X/Fe]$ ratio that could be attributed to uncertainties in the model at-

mosphere parameters. For example, these values are 0.11 and 0.12 dex for $[La/Fe]$ and $[Eu/Fe]$. The standard deviations of the $[La/Fe]$ and $[Eu/Fe]$ ratios are each 0.13 dex. The comparable magnitudes of these values suggest that the correlated heavy element abundance ratios may not have a cosmic origin.

To demonstrate this point, we perform the following test. Using the values presented in Table 9, we adjust the T_{eff} values for each star to force the individual $[Eu/Fe]$ ratios to equal the mean $[Eu/Fe]$ ratio. We then apply these T_{eff} adjustments to the individual $[La/Fe]$ ratios to derive revised $[La/Fe]$ ratios for each star. The standard deviation of the revised $[La/Fe]$ ratios is 30 per cent smaller than the standard deviation of the uncorrected ratios. Other rare earth elements exhibit similar responses. We conclude from this test that random errors in T_{eff} can account for a substantial portion of the dispersion, and we infer that random errors in the other model atmosphere parameters may have similar impact.

All of the heavy-element ratios shown to correlate in Figure 14 are derived from ionized atoms, so other elements detected as ions (Sc, Ti, V, and Cr) might exhibit similar characteristics. However, Table 9 indicates that the $[Sc\ II/Fe]$, $[Ti\ II/Fe]$, $[V\ II/Fe]$, and $[Cr\ II/Fe]$ should not be expected to behave like, e.g., $[La\ II/Fe]$ or $[Eu\ II/Fe]$. For example, $\delta[Ti\ II/Fe]/\delta v_t = -0.04$, while $\delta[La\ II/Fe]/\delta v_t = +0.05$. Responses to δT_{eff} and $\delta \log g$ are also dissimilar. Even though both ratios are derived from lines of ionized atoms, the line strengths and excitation potentials are different. The excitation potentials of Sc II, Ti II, V II, and Cr II lines used range from 1.08 to 4.07 eV with a median of 1.50 eV, while the excitation potentials of the heavy rare earth elements’ lines range from 0.00 to 1.38 eV with a median of 0.32 eV. This difference is significant. The $[Sc\ II/Fe]$, $[Ti\ II/Fe]$, $[V\ II/Fe]$, and $[Cr\ II/Fe]$ ratios are not a good control group for $[La\ II/Fe]$ or $[Eu\ II/Fe]$, as was assumed by Roederer (2011).

We conclude that there is no compelling evidence of a cosmic origin for the correlations among pairs of n -capture-element ratios in NGC 4833. The detected correlations likely result from random errors in the model atmosphere parameters. We suggest that the correlations identified among literature data by Roederer (2011) may also be the result of similar random errors in the model atmosphere parameters. The r -process dispersion in M15, however, is too large (> 0.7 dex) to be explained entirely by this phenomenon, and we note that Tsujimoto & Shigeyama (2014) have recently offered a theoretical explanation of its origin.

9.6 The ^{232}Th nuclear chronometer in NGC 4833

We derive upper limits on the Th abundance based on the non-detection of the Th II line at 4019 Å. This line originates from radioactive ^{232}Th , which can only be produced via r -process nucleosynthesis. This upper limit sets a lower limit on the age of the r -process material in NGC 4833. We compare the Th abundance to Eu, a well-measured, stable element presumably produced by the same nucleosynthesis channel. The lowest Th/Eu ratio found in NGC 4833, in star 2-1664, is $\log \epsilon(\text{Th}/\text{Eu}) < -0.47 \pm 0.09$. If we assume the Th and Eu were produced in the ratio reported in Table 9 of Roederer et al. (2009), this implies an age greater than

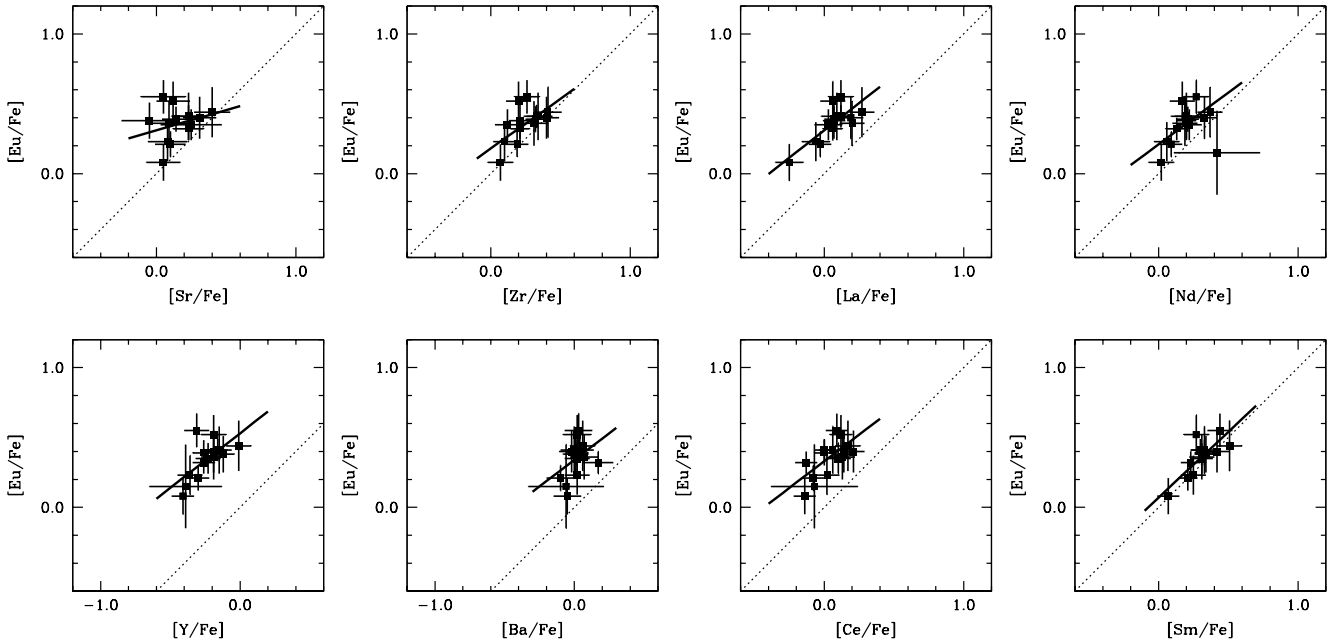


Figure 14. Correlations among heavy element ratios in NGC 4833 for elements measured in 14 or more stars. The red lines mark the weighted least-squares fits. Dotted lines mark the solar values. We have checked, and confirmed, the weighted fit for $[\text{Ba}/\text{Fe}]$ versus $[\text{Eu}/\text{Fe}]$, which appears to deviate from what might be expected from a by-eye fit. The uncertainty on this fit is considerably larger than for the other rare earth elements, as can be seen in Figure 15.

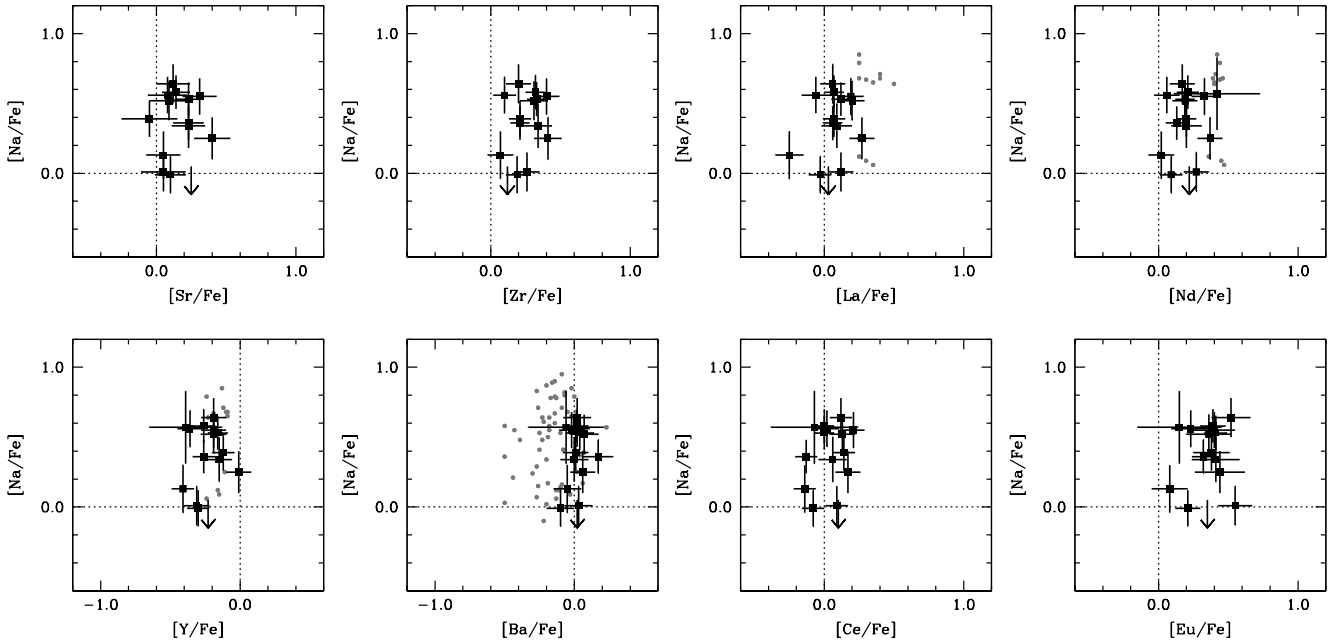


Figure 16. Relationships among heavy elements and $[\text{Na}/\text{Fe}]$ in NGC 4833. Black points mark our derived abundance ratios, and gray circles mark those from Carretta et al. (2014). Dotted lines mark the solar values. No correlations are apparent.

6.4 Gyr. This value is not very constraining, but it implies that the r -process material in NGC 4833 is not young.

Alternatively, we could assume that NGC 4833 is old (Melbourne et al. 2000; Marín-Franch et al. 2009) and treat the initial Th/Eu production ratio as a free parameter. An assumed age of 12 ± 1.5 Gyr implies an initial production ratio of $\log \epsilon(\text{Th}/\text{Eu}) = -0.21 \pm 0.09$. This implies that the r -process material was not produced in an “actinide

boost” event (cf. Hill et al. 2002; Schatz et al. 2002), which would require an initial production ratio of $\log \epsilon(\text{Th}/\text{Eu}) = +0.11 \pm 0.07$ to yield an age consistent with the prototype actinide boost halo star CS 31082–001.

To the best of our knowledge, no actinide boost has yet been observed in any globular cluster star. ^{232}Th has been detected in globular clusters M5 (Lai et al. 2011), M15 (Snedden et al. 2000), M22 (Roederer et al. 2011), and

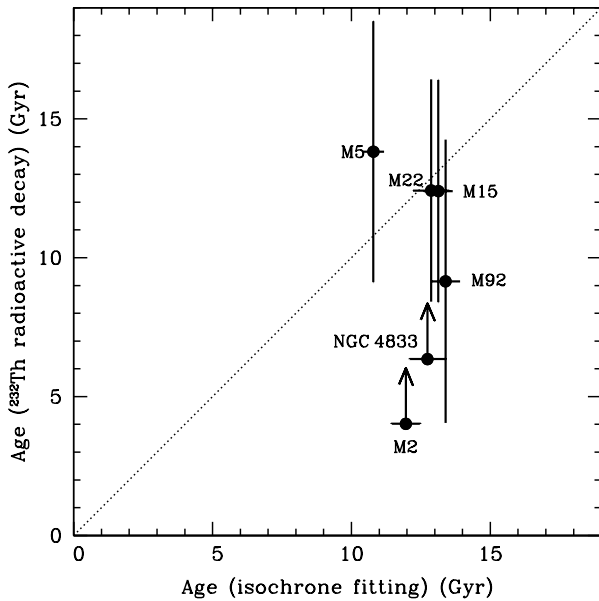


Figure 17. Comparison of globular cluster ages derived from isochrone fitting and radioactive decay of ^{232}Th . The relative ages presented by Marín-Franch et al. (2009) are based on stellar evolution models by Dotter et al. (2007) and have been normalized to an absolute age of 13.0 Gyr. The dotted line marks the 1:1 correspondence.

M92 (Johnson & Bolte 2001). We also report an unpublished upper limit on ^{232}Th in M2, $\log \epsilon(\text{Th}/\text{Eu}) < -0.42$, based on spectra obtained by I.U.R. and published in Yong et al. (2014). Ages calculated from the $\log \epsilon(\text{Th}/\text{Eu})$ ratios are consistent with ages deduced by isochrone fitting (Marín-Franch et al. 2009), as shown in Figure 17.² The uncertainties are substantial, but we would expect to find values in the lower right corner of Figure 17 if an actinide boost is present in any of these six clusters at the level found in CS 31082–001. No detections are found here.

The astrophysical site(s) responsible for r -process nucleosynthesis are still debated. Non-detection of the actinide boost in globular clusters may provide a new environmental test of r -process nucleosynthesis models. The sample of clusters where ^{232}Th has been studied is still small, however, so new data are of great importance.

10 CONCLUSIONS

We have collected new high-resolution spectroscopic observations of 15 giants in the metal-poor globular cluster NGC 4833. We derive stellar parameters for these stars and examine up to 354 lines of 48 species of 44 elements in each star. We detect 43 species of 39 elements and present upper limits derived from the non-detections of the others. Overall, the composition of stars in NGC 4833 appears relatively normal for a metal-poor globular cluster.

We derive a mean metallicity of $\langle [\text{Fe}/\text{H}] \rangle =$

-2.25 ± 0.02 ($\sigma = 0.09$) from Fe I lines and $\langle [\text{Fe}/\text{H}] \rangle = -2.19 \pm 0.013$ ($\sigma = 0.05$) from Fe II lines. These uncertainties support the results of Carretta et al. (2014) that there is no internal Fe dispersion within NGC 4833. Our derived mean metallicity is 0.20 ± 0.02 dex lower than that derived by Carretta et al. for four stars in common. We derive $[\text{Fe}/\text{H}] = -2.19 \pm 0.04$ for NGC 4833 on the differential globular cluster scale established by Koch & McWilliam (2008, 2011) relative to the K-giant Arcturus, which supports our lower metallicity.

Our data reveal the abundance variations among $[\text{O}/\text{Fe}]$, $[\text{Na}/\text{Fe}]$, $[\text{Mg}/\text{Fe}]$, $[\text{Al}/\text{Fe}]$, and possibly $[\text{Si}/\text{Fe}]$ commonly found in globular clusters. There are bi-modal distributions among the $[\text{Na}/\text{Fe}]$, $[\text{Mg}/\text{Fe}]$, and $[\text{Al}/\text{Fe}]$ ratios. Our results reaffirm those of Carretta et al. (2014). We also reproduce a hint of an anti-correlation between $[\text{Si}/\text{Fe}]$ and $[\text{Mg}/\text{Fe}]$, but our data do not reveal statistically-significant correlations between $[\text{Si}/\text{Fe}]$ and either $[\text{Na}/\text{Fe}]$ or $[\text{Al}/\text{Fe}]$. We suspect the discrepancy between our data and Carretta et al. is a result of the smaller sample size examined by us.

Quantitative measures of potential anti-correlations between $[\text{K}/\text{Fe}]$ and $[\text{Mg}/\text{Fe}]$ and between $[\text{Sc}/\text{Fe}]$ and $[\text{Mg}/\text{Fe}]$ reveal that neither is significant. Furthermore, neither $[\text{K}/\text{Fe}]$ nor $[\text{Sc}/\text{Fe}]$ correlate with $[\text{Na}/\text{Fe}]$, $[\text{Al}/\text{Fe}]$, or $[\text{Si}/\text{Fe}]$ at the 2σ level. Our data demonstrate that NGC 4833 does not possess the extreme relations among $[\text{Mg}/\text{Fe}]$, $[\text{K}/\text{Fe}]$, and $[\text{Sc}/\text{Fe}]$ found in the globular clusters NGC 2419 and NGC 2808. We find no dispersion among any of the other iron-group elements in NGC 4833.

We detect up to 20 n -capture elements in NGC 4833, and we place upper limits on four others. Abundances of the rare earth elements are consistent with r -process nucleosynthesis. Sr, Y, Zr, Mo, and Ba are enhanced relative to the scaled solar r -process distribution, but low levels of Yb, Hf, and Pb suggest that this is not due to enrichment by the s -process. Instead, the weak and main components of the r -process may be responsible. The heavy-element abundance distribution in NGC 4833 closely resembles that found in M5, M15, M92, NGC 2419, and the r -process-only stellar groups in M2 and M22. There is no correlation between the n -capture elements and the light-element variations in NGC 4833, which reaffirms and expands upon results obtained by Carretta et al. (2014). Our analysis of correlations between $[\text{La}/\text{Fe}]$, $[\text{Eu}/\text{Fe}]$, and other n -capture elements in NGC 4833 reveals that they are likely due to random errors in the stellar parameters, and we conclude that there is no compelling evidence for cosmic dispersion among the heavy elements in NGC 4833. This cluster does not possess wide star-to-star variations like those observed in ω Cen, M2, M15, M22, or NGC 1851.

Upper limits derived from the non-detection of the Th II line at 4019 Å indicate that the r -process material in NGC 4833 was not formed in an actinide boost event. No other clusters that have been studied show evidence of an actinide boost, either. The potential non-detection of the actinide boost in globular clusters presents a new environmental test of r -process nucleosynthesis models that should be investigated further.

² Yong et al. (2008a,b) detected Th in M4 and M5, but the high $[\text{Th}/\text{Fe}]$ ratio in M5 derived by Yong et al. was not confirmed by Lai et al. (2011). We refrain from drawing any conclusions from the $[\text{Th}/\text{Fe}]$ ratios presented by Yong et al.

ACKNOWLEDGMENTS

I.U.R. thanks E. Carretta for sending equivalent width measurements and D. Yong for advice during the early stages of the analysis. We appreciate the helpful suggestions and rapid response of the referee. This research has made use of NASA's Astrophysics Data System bibliographic services, the arXiv preprint server operated by Cornell University, the SIMBAD and VizieR databases hosted by the Strasbourg Astronomical Data Center, the Atomic Spectra Database (Kramida et al. 2013) hosted by the National Institute of Standards and Technology, and the Two Micron All Sky Survey, which is a joint project of the University of Massachusetts and the Infrared Processing and Analysis Center/California Institute of Technology, funded by the National Aeronautics and Space Administration and the National Science Foundation. IRAF is distributed by the National Optical Astronomy Observatories, which are operated by the Association of Universities for Research in Astronomy, Inc., under cooperative agreement with the National Science Foundation.

REFERENCES

- Aldenius M., Lundberg H., Blackwell-Whitehead R. 2009, *A&A*, 502, 989
- Allen C., Moreno E., Pichardo B. 2008, *ApJ*, 674, 237
- Alonso A., Arribas S., Martínez-Roger C. 1999a, *A&AS*, 139, 335
- Alonso A., Arribas S., Martínez-Roger C. 1999b, *A&AS*, 140, 261
- Asplund M., Grevesse N., Sauval A. J., Scott P. 2009, *ARA&A*, 47, 481
- Bernstein R., Shectman S. A., Gunnels S. M., Mochnacki S., Athey A. E. 2003, *Proc. SPIE*, 4841, 1694
- Biémont É., Garnir H. P., Palmeri P., Li Z. S., Svanberg S. 2000, *MNRAS*, 312, 116
- Biémont É., et al. 2011, *MNRAS*, 414, 3350
- Bisterzo S., Gallino R., Straniero O., Cristallo S., Käppeler F. 2010, *MNRAS*, 404, 1529
- Bisterzo S., Gallino R., Straniero O., Cristallo S., Käppeler F. 2011, *MNRAS*, 418, 284
- Bohlin, R. C., Hill, J. K., Jenkins, E. B., et al. 1983, *ApJS*, 51, 277
- Bressan A., Marigo P., Girardi L., Salasnich B., Dal Cero C., Rubele S., Nanni A. 2012, *MNRAS*, 427, 127
- Busso M., Gallino R., Wasserburg G. J. 1999, *ARA&A*, 37, 239
- Cardelli J. A., Clayton G. C., Mathis J. S. 1989, *ApJ*, 345, 245
- Carretta E., Gratton R., Cohen J. G., Beers T. C., Christlieb N. 2002, *AJ*, 124, 481
- Carretta E., Bragaglia A., Gratton R. G., Lucatello S., Momany Y. 2007, *A&A*, 464, 927
- Carretta E. et al. 2009a, *A&A*, 505, 117
- Carretta E., Bragaglia A., Gratton R., Lucatello S. 2009b, *A&A*, 505, 139
- Carretta E., Lucatello S., Gratton R. G., Bragaglia A., D'Orazi V. 2011, *A&A*, 533, A69
- Carretta E., Gratton R. G., Bragaglia A., D'Orazi V., Lucatello S., Sollima A., Sneden C. 2013, *ApJ*, 769, 40
- Carretta E. et al. 2014, *A&A*, 564, A60
- Casetti-Dinescu D. I., Girard T. M., Herrera D., van Alena W. F., López C. E., Castillo D. J. 2007, *AJ*, 134, 195
- Castelli F., Kurucz R. L. *Proc. IAU Symp. No 210, Modelling of Stellar Atmospheres*, eds. N. Piskunov et al. 2003, A20
- Cayrel R. et al. 2004, *A&A*, 416, 1117
- Chen Y., Girardi L., Bressan A., Marigo P., Barbieri M., Kong X. 2014, *MNRAS*, 444, 2525
- Cohen J. G. 2011, *ApJL*, 740, L38
- Cohen J. G., Kirby E. N. *ApJ*, 760, 86
- Cohen J. G., Huang W., Kirby E. N. 2011, *ApJ*, 740, 60
- Cowan J. J., et al. 2005, *ApJ*, 627, 238
- Cox, A. N., ed. 2000, *Allen's Astrophysical Quantities*, Springer-Verlag, New York, p. 340–341
- Den Hartog E. A., Lawler J. E., Sneden C., Cowan J. J. 2003, *ApJS*, 148, 543
- Den Hartog E. A., Lawler J. E., Sneden C., Cowan J. J. 2006, *ApJS*, 167, 292
- Den Hartog E. A., Lawler J. E., Sobeck J. S., Sneden C., Cowan J. J. 2011, *ApJS*, 194, 35
- Doerr A., Kock M., Kwiatkowski M., Werner K. 1985, *J. Quant. Spectrosc. Rad. Trans.*, 33, 55
- Dotter A., Chaboyer B., Jevremović D., Baron E., Ferguson J. W., Sarajedini A., Anderson J. 2007, *AJ*, 134, 376
- Fabbian D., Asplund M., Barklem P. S., Carlsson M., Kiselman D. 2009, *A&A*, 500, 1221
- Frebel, A., Collet, R., Eriksson, K., Christlieb, N., Aoki, W. 2008a, *ApJ*, 684, 588
- Fuhr J. R., Wiese W. L. 2009, *Atomic Transition Probabilities*, published in the CRC Handbook of Chemistry and Physics, 90th Edition, ed. Lide, D. R., CRC Press, Inc., Boca Raton, FL, 10-93
- García Pérez A. E., Asplund M., Primas F., Nissen P. E., Gustafsson B. 2006, *A&A*, 451, 621
- Geisler D., Piatti A. E., Claria J. J., Minniti D. 1995, *AJ*, 109, 605
- Gratton R. G., Ortolani S. 1989, *A&A*, 211, 41
- Gratton R., Sneden C., Carretta E. 2004, *ARA&A*, 42, 385
- Gratton R. G., Carretta E., Claudi R., Lucatello S., Barbieri M. 2003, *A&A*, 404, 187
- Gratton, R. G. et al. 2007, *A&A*, 464, 953
- Harris W. E. 1996, *AJ*, 112, 1487
- Hill V., et al. 2002, *A&A*, 387, 560
- Honda S. et al. 2004, *ApJS*, 152, 113
- Honda S., Aoki W., Ishimaru Y., Wanajo S., Ryan S. G. 2006, *ApJ*, 643, 1180
- Isobe T., Feigelson E. D., Nelson P. I. 1986, *ApJ*, 306, 490
- Ivans I. I., Sneden C., James C. R., Preston G. W., Fulbright J. P., Höflich P. A., Carney B. W., Wheeler, J. C. 2003, *ApJ*, 592, 906
- Ivans I. I., Simmerer J., Sneden C., Lawler J. E., Cowan J. J., Gallino R., Bisterzo S. 2006, *ApJ*, 645, 613
- Ivarsson S., Litzén U., Wahlgren G. M. 2001, *Phys. Scr.*, 64, 455
- Ivarsson S., et al. 2003, *A&A*, 409, 1141
- Johnson J. A. 2002, *ApJS*, 139, 219
- Johnson J. A., Bolte M. 2001, *ApJ*, 554, 888
- Kelson D. D. 2003, *PASP*, 115, 688
- Kiselman D. 2001, *New Astronomy Reviews*, 45, 559
- Koch A., McWilliam A. 2008, *AJ*, 135, 1551
- Koch A., McWilliam A. 2011, *AJ*, 142, 63

- Kraft R. P., Peterson R. C., Guhathakurta P., Sneden C., Fulbright J. P., Langer G. E. 1999, *ApJL*, 518, L53
- Kramida A. et al. 2013, NIST Atomic Spectra Database (version 5.1), available online: <http://physics.nist.gov/asd>
- Kurucz R. 1993, ATLAS9 Stellar Atmosphere Programs and 2 km/s grid, CD-ROM 13
- Kurucz R. L., Bell B. 1995, Cambridge, MA: Smithsonian Astrophysical Observatory, CD-ROM 23
- Lai D. K., Bolte M., Johnson J. A., Lucatello S., Heger A., Woosley S. E. 2008, *ApJ*, 681, 1524
- Lai D. K., Smith G. H., Bolte M., Johnson J. A., Lucatello S., Kraft R. P., Sneden C. 2011, *AJ*, 141, 62
- Lardo C., et al. 2015, *A&A*, 573, A115
- Lavalley M. P., Isobe T., Feigelson E. D. 1992, *Bull. Am. Astronom. Soc.*, 24, 839
- Lawler J. E., Dakin J. T. 1989, *J. Opt. Soc. Am. B Optical Physics*, 6, 1457
- Lawler J. E., Bonvallet G., Sneden C. 2001, *ApJ*, 556, 452
- Lawler J. E., Sneden C., Cowan J. J. 2004, *ApJ*, 604, 850
- Lawler J. E., Wyart J.-F., Blaise J. 2001, *ApJS*, 137, 351
- Lawler J. E., Wickliffe M. E., Den Hartog E. A., Sneden C. 2001a, *ApJ*, 563, 1075
- Lawler J. E., Wickliffe M. E., Cowley C. R., Sneden C. 2001b, *ApJS*, 137, 341
- Lawler J. E., Den Hartog E. A., Sneden C., Cowan J. J. 2006, *ApJS*, 162, 227
- Lawler J. E., Den Hartog E. A., Labby Z. E., Sneden C., Cowan J. J., Ivans I. I. 2007, *ApJS*, 169, 120
- Lawler J. E., Sneden C., Cowan J. J., Wyart J.-F., Ivans I. I., Sobeck J. S., Stockett M. H., Den Hartog E. A. 2008, *ApJS*, 178, 71
- Lawler J. E., Sneden C., Cowan J. J., Ivans I. I., Den Hartog E. A. 2009, *ApJS*, 182, 51
- Lawler J. E., Guzman A., Wood M. P., Sneden C., Cowan J. J. 2013, *ApJS*, 205, 11
- Li R., Chatelain R., Holt R. A., Rehse S. J., Rosner S. D., Scholl T. J. 2007, *Phys. Scr.*, 76, 577
- Lind K., Asplund M., Barklem P. S. 2009, *A&A*, 503, 541
- Lind K., Asplund M., Barklem P. S., Belyaev A. K. 2011, *A&A*, 528, A103
- Ljung G., Nilsson H., Asplund M., Johansson S. 2006, *A&A*, 456, 1181
- Marín-Franch A. et al. 2009, *ApJ*, 694, 1498
- Marino A. F., Milone A. P., Piotto G., Villanova S., Bedin L. R., Bellini A., Renzini A. 2009, *A&A*, 505, 1099
- Marino A. F. et al. 2011, *A&A*, 532, A8
- McWilliam, A., Preston, G. W., Sneden, C., & Searle, L. 1995, *AJ*, 109, 2757
- McWilliam A. 1998, *AJ*, 115, 1640
- Melbourne J., Sarajedini A., Layden A., Martins D. H. 2000, *AJ*, 120, 3127
- Menzies J. 1972, *MNRAS*, 156, 207
- Minniti D., Geisler D., Peterson R. C., Claria J. J. 1993, *ApJ*, 413, 548
- Minniti D., Peterson R. C., Geisler D., Claria J. J. 1996, *ApJ*, 470, 953
- Monaco L., Pancino E., Ferraro F. R., Bellazzini M. 2004, *MNRAS*, 349, 1278
- Mucciarelli A., Bellazzini M., Ibata R., Merle T., Chapman S. C., Dalessandro E., Sollima A. 2012, *MNRAS*, 426, 2889
- Mucciarelli A., Bellazzini M., Merle T., Plez B., Dalessandro E., Ibata R. 2015, *ApJ*, in press (arXiv:1501.03161)
- Nilsson H., Zhang Z. G., Lundberg H., Johansson S., Nordström, B. 2002, *A&A*, 382, 368
- Nilsson H., Ljung G., Lundberg H., Nielsen K. E. 2006, *A&A*, 445, 1165
- Nilsson H., et al. 2010, *A&A*, 511, A16
- Norris J. E., Da Costa G. S. 1995, *ApJ*, 447, 680
- Otsuki K., Honda S., Aoki W., Kajino T., Mathews G. J. 2006, *ApJL*, 641, L117
- Palmeri P., Fischer C. F., Wyart J.-F., Godefroid M. R. 2005, *MNRAS*, 363, 452
- Pilachowski C. A., Sneden C., Wallerstein G. 1983, *ApJS*, 52, 241
- Piotto G., et al. 2002, *A&A*, 391, 945
- Preston G. W., Sneden C., Thompson I. B., Sheckman S. A., Burley G. S. 2006, *AJ*, 132, 85
- Ramírez I., Meléndez J. 2005, *ApJ*, 626, 446
- Roederer I. U. 2011, *ApJL*, 732, L17
- Roederer I. U., Lawler J. E. 2012, *ApJ*, 750, 76
- Roederer I. U., Sneden C. 2011, *AJ*, 142, 22
- Roederer I. U., Marino A. F., Sneden C. 2011, *ApJ*, 742, 37
- Roederer I. U., Lawler J. E., Sneden C., Cowan J. J., Sobeck J. S., Pilachowski C. A. 2008, *ApJ*, 675, 723
- Roederer I. U., Kratz K.-L., Frebel A., Christlieb N., Pfeiffer B., Cowan J. J., Sneden C. 2009, *ApJ*, 698, 1963
- Roederer I. U., Cowan J. J., Karakas A. I., Kratz K.-L., Lugaro M., Simmerer J., Farouqi K., Sneden C. 2010, *ApJ*, 724, 975
- Roederer I. U., et al. 2012, *ApJS*, 203, 27
- Roederer I. U., Preston G. W., Thompson I. B., Sheckman S. A., Sneden C., Burley G. S., Kelson D. D. 2014, *AJ*, 147, 136
- Ruffoni M. P., Den Hartog E. A., Lawler J. E., Brewer N. R., Lind K., Nave G., Pickering J. C. 2014, *MNRAS*, 441, 3127
- Rutledge G. A., Hesser J. E., Stetson P. B., Mateo M., Simard L., Bolte M., Friel E. D., Copin Y. 1997, *PASP*, 109, 883
- Samus N., Kravtsov V., Pavlov M., Alcaïno G., Liller W. 1995, *A&AS*, 109, 479
- Schatz H., Toenjes R., Pfeiffer B., Beers T. C., Cowan J. J., Hill V., Kratz K.-L. 2002, *ApJ*, 579, 626
- Skrutskie M. F., et al. 2006, *AJ*, 131, 1163
- Smith V. V., Lambert D. L., Nissen P. E. 1998, *ApJ*, 506, 405
- Smith V. V., Shetrone M. D., Keane M. J. 1999, *ApJL*, 516, 73
- Smith V. V., Suntzeff N. B., Cunha K., Gallino R., Busso M., Lambert D. L., Straniero O. 2000, *AJ*, 119, 1239
- Sneden C. A. 1973, Ph.D. Thesis, Univ. of Texas at Austin
- Sneden C., Pilachowski C. A., Kraft R. P. 2000, *AJ*, 120, 1351
- Sneden C., Kraft R. P., Shetrone M. D., Smith G. H., Langer G. E., Prosser C. F. 1997, *AJ*, 114, 1964
- Sneden C., et al. 2003, *ApJ*, 591, 936
- Sneden C., Cowan J. J., Gallino R. 2008, *ARA&A*, 46, 241
- Sneden C., Lawler J. E., Cowan J. J., Ivans I. I., Den Hartog E. A. 2009, *ApJS*, 182, 80
- Sobeck J. S., Lawler J. E., Sneden C. 2007, *ApJ*, 667, 1267
- Sobeck J. S., et al. 2011, *AJ*, 141, 175
- Takeda Y., Zhao G., Chen Y.-Q., Qiu H.-M., Takada-Hidai M. 2002, *PASJ*, 54, 275

- Tsujimoto T., Shigeyama T. 2014, *ApJ*, 795, L18
Wickliffe M. E., Lawler J. E. 1997, *J. Opt. Soc. Am. B Optical Physics*, 14, 737
Wickliffe M. E., Lawler J. E., Nave G. 2000, *J. Quant. Spectrosc. Rad. Trans.*, 66, 363
Wood M. P., Lawler J. E., Sneden C., Cowan J. J. 2013, *ApJS*, 208, 27
Wood M. P., Lawler J. E., Sneden C., Cowan J. J. 2014a, *ApJS*, 211, 20
Wood M. P., Lawler J. E., Den Hartog E. A., Sneden C., Cowan J. J. 2014b, *ApJS*, 214, 18
Worley C. C., Hill V., Sobek J., Carretta E. 2013, *A&A*, 553, A47
Yong D., Grundahl F., Nissen P. E., Jensen H. R., Lambert D. L. 2005, *A&A*, 438, 875
Yong D., Grundahl F. 2008, *ApJ*, 672, L29
Yong D., Lambert D. L., Paulson D. B., Carney B. W. 2008a, *ApJ*, 673, 854
Yong D., Karakas A. I., Lambert D. L., Chieffi A., Limongi M. 2008b, *ApJ*, 689, 1031
Yong D., Grundahl F., Lambert D. L., Nissen P. E., Shetrone M. D. 2003, *A&A*, 402, 985
Yong D., et al. 2014, *MNRAS*, 441, 3396